J. Fluid Mech. (1997), *vol.* 348, *pp.* 201–245. Printed in the United Kingdom

Local isotropy in complex turbulent boundary layers at high Reynolds number

By SEYED G. SADDOUGHI†

Center for Turbulence Research, Bldg 500, Stanford University, CA 94305, USA and NASA Ames Research Center, Moffett Field, CA 94035, USA

(Received 20 January 1997)

To continue our (Saddoughi & Veeravalli 1994) tests of the local-isotropy predictions of Kolmogorov's (1941) universal equilibrium theory in shear flows, we have taken hot-wire measurements of the velocity fluctuations in complex turbulent boundary layers at several Reynolds numbers. We have studied the plane-of-symmetry flow upstream of a 4 ft diameter, 6 ft long circular cylinder placed with its axis vertical in the zero-pressure-gradient turbulent boundary layer of the test-section ceiling in the 80 ft × 120 ft Full-Scale Aerodynamics Facility at NASA Ames Research Center.

In the present experiments, the pressure rises strongly as the obstacle is approached and in and near the plane of symmetry of the flow the boundary layer is influenced by the effects of lateral divergence. In addition to the basic mean shear, $\partial U/\partial y$, the extra mean strain rates are $\partial U/\partial x$, $\partial V/\partial y$ and $\partial W/\partial z$. During our experiments a full-scale F-18 fighter aircraft, set at an angle of attack of 50°, was present in the central region of the working section. To identify the effects of the aircraft on the boundary-layer characteristics upstream of the cylinder, we have also taken measurements when the wind tunnel was empty. It appears that the presence of the aircraft in the wind tunnel usefully increases the magnitude of the mean strain rates, and also significantly increases the large-scale intermittency near the edge of the boundary layer upstream of the cylinder. The maximum values for the parameters that have been found to represent the effects of mean shear on turbulence are $S^*(\equiv Sq^2/\varepsilon) \approx 22$ and $S_c^*(\equiv S(\nu/\varepsilon)^{1/2}) \approx 0.05$, where for the present experiments $S \equiv 2(s_{ij}s_{ij}/2)^{1/2}$.

All of the present results are compared with our plane turbulent boundary-layer experiments (Saddoughi & Veeravalli 1994). In the present distorted boundary-layer cases, the maximum Reynolds numbers based on momentum thickness, R_θ, and on the Taylor (1935) microscale, R_λ, are increased to approximately 510 000 and 2000 respectively. These are the largest attained in laboratory boundary-layer flows: R_θ is of the same order obtained in flight on a typical commercial aircraft or the space shuttle.

In general, the current investigations confirm the conclusions of our earlier study. In summary, it is shown again that one decade of locally isotropic inertial subrange requires a ratio of the Kolmogorov to mean-shear timescales, S_c^*, of not more than approximately 0.01. In the present non-equilibrium shear layer, this was achieved at a microscale Reynolds number of approximately 2000.

---

† Present address: General Electric Corporate Research & Development, K-1, ES-210, One Research Circle, P.O. Box 8, Schenectady, NY 12301, USA.

1. Introduction

During the last few years, we (Saddoughi 1993, 1994, 1995; Saddoughi & Veeravalli 1994, hereinafter referred to as I) have conducted high- and low-Reynolds-number experiments and taken hot-wire measurements of the three components of the velocity fluctuations in the test-section-ceiling boundary layer of the 80×120 foot Full-Scale Aerodynamics Facility at NASA Ames Research Center. The ceiling has acoustic treatment which has the same effect as surface roughness. The purpose of these experiments was to test the local-isotropy predictions of Kolmogorov's (1941) universal equilibrium theory, which states that at sufficiently high Reynolds numbers the small-scale structures of turbulent motions are independent of the large-scale structures and mean deformations. Our goal was to obtain accurate small-scale data in a variety of flows in the hope that the analysis of these experimental data would enhance our understanding of the local-isotropy hypothesis. To achieve this goal, our experiments were divided into two sets.

Our first set of measurements was taken at several Reynolds numbers in a plane turbulent boundary layer, a 'simple' shear flow with the basic mean strain rate $S \equiv \partial U/\partial y$. Note that the coordinate system, the symbols used for different variables and the equations describing the theoretical background for the local-isotropy hypothesis are all given in I and will not be repeated here. In the 80 ft $\times$ 120 ft wind tunnel the ceiling boundary-layer thickness at our measurement location was approximately 1.1 m for the plane-flow experiments and the maximum Reynolds numbers based on momentum thickness R_θ, and on Taylor (1935) microscale, R_λ, were 370 000 and 1500 respectively. As mentioned above, the boundary layer developed over a rough surface, but the Reynolds-stress profiles agreed with canonical data sufficiently well for our purposes. Spectral and structure-function relations for isotropic turbulence were used to test the local-isotropy hypothesis, and our results have established the condition under which local isotropy can be expected in simple shear flows. To within the accuracy of measurement, the shear-stress cospectral density $E_{12}(k_1)$ fell to zero at a wavenumber about one decade *larger* than that at which the energy spectra first followed the $-\frac{5}{3}$ power law. At the highest Reynolds number, $E_{12}(k_1)$ vanished about one decade *before* the start of the dissipation range and remained zero in the dissipation range.

We showed that the lower wavenumber limit of locally-isotropic behaviour of the shear-stress cospectra is $k_1(\varepsilon/S^3)^{1/2} \approx 10$. Our investigation also indicated that for energy spectra this limit could be relaxed to $k_1(\varepsilon/S^3)^{1/2} \approx 3$; this is Corrsin's (1958) criterion, with the numerical value obtained from our data. The existence of an isotropic inertial range requires that this wavenumber be much less than the wavenumber at the onset of viscous effects, $k_1\eta \ll 1$, so that the combined condition (Corrsin 1958 and Uberoi 1957) is $S(\nu/\varepsilon)^{1/2} \ll 1$. It was observed that in the dissipation range the energy spectra had a simple exponential decay (Kraichnan 1959) with an exponent prefactor close to the value $\beta = 5.2$ obtained in direct numerical simulations at low Reynolds number. The inertial-range constant for the three-dimensional spectrum, C, was estimated to be 1.5 ± 0.1 (Monin & Yaglom 1975). Spectral 'bumps' between the $-\frac{5}{3}$ inertial range and the dissipative range were observed in all of the compensated energy spectra. The shear-stress cospectra rolled-off with a $-\frac{7}{3}$ power law before the start of local isotropy in the energy spectra, and scaled linearly with S (Lumley 1967). The constant for the cospectra was estimated to be $C_0 \approx 0.15$ (Wyngaard & Cote 1972). Overall, it was shown that one decade of isotropic inertial subrange requires $S(\nu/\varepsilon)^{1/2}$, to be not more than about 0.01: for a simple shear layer with turbulent kinetic energy production approximately equal to dissipation, this implies a microscale Reynolds number of about 1500.

In I, we presented a brief review of the previous experimental and computational investigations of the local-isotropy hypothesis. Since then there have been further experimental studies of high-Reynolds-number shear flows: for example, Fernholz *et al.* (1995) (large-scale turbulence and some spectral measurements in the wall boundary layer of a large wind tunnel); D. B. DeGraaff & J. K. Eaton (1996, personal communication) (large-scale turbulence measurements in the wall boundary layer of a pressurized wind tunnel); Zagarola *et al.* (1996) (mean-flow measurements in the turbulent flow of a pressurized pipe); Miller & Dimotakis (1996) (scalar spectral measurements in high-Schmidt-number turbulent jets).

There have also been a number of excellent review articles. Bradshaw (1994) reviews current topics in turbulence research, from very basic questions of turbulence theory to the important practical question of the reliability of turbulence models, and gives examples of popular fallacies about the behaviour of turbulence.

Gad-el-Hak & Bandyopadhyay (1994) and Fernholz & Finley (1996) review the available data in wall-bounded turbulent flows and present very comprehensive discussions of the Reynolds-number effects in these types of flows. In general they conclude that the mean-flow and large-scale turbulent characteristics at high Reynolds numbers are poorly understood and that further experimental investigations are needed.

Nelkin's (1994) extensive review of the experimental and numerical-simulation data concludes that the small-scale velocity fluctuations in high-Reynolds-number incompressible turbulent flows exhibit universal behaviour independent of the large-scale structure. He also emphasizes the need for a fundamental theoretical insight into the problem of turbulence, the lack of which has hampered progress in solving this problem for so long (recently, some advances have been made in this direction by Hill & Wilczak 1995, Lindborg 1995, 1996 and Frisch 1995).

To examine the universality of the Kolmogorov constant for the longitudinal spectra C_1 (see I, equation 7), Sreenivasan (1995) reviewed an extensive set of available data from experiments that were conducted in a variety of flows (grid turbulence, wall-bounded and free shear flows, and geophysical flows) over a very large range of Reynolds numbers ($28 \leqslant R_\lambda \leqslant 18\,000$). He concluded that all the data for $R_\lambda > 50$ (see also Bradshaw 1969) essentially indicate $C_1 \approx 0.5$, independent of the flow and the Reynolds number, which is the accepted value for this constant (Monin & Yaglom 1975). It is appropriate here to mention that a very informative review paper by Yaglom (1994), which covers Kolmogorov's scientific and social activities, providing a complement to the volume of articles in the *Proceedings of the Royal Society*, dedicated to the 50th anniversary of Kolmogorov's ideas (Hunt, Phillips & Williams 1991).

However, Mydlarski & Warhaft (1996), who took spectral measurements in grid-generated wind tunnel turbulence in the range $50 \leqslant R_\lambda \leqslant 473$, conclude that not only is the Kolmogorov constant a weak function of Reynolds number, so too is the Kolmogorov power-law exponent (nominally $-\frac{5}{3}$) in the inertial subrange: they propose that the accepted values are obtained only above $R_\lambda \approx 10\,000$.

Low-Reynolds-number ($40 \leqslant R_\lambda \leqslant 260$) measurements on the centrelines of turbulent wakes behind circular cylinders by Antonia *et al.* (1996) and Antonia, Zhu & Shafi (1996) show agreement with local-isotropy predictions for second-order velocity and temperatur structure functions, and vorticity spectra. However, they indicate that second- and fourth-order moments of vorticity show departures from local isotropy, independent of Reynolds number.

Based on the results of their simulations of homogeneous shear flows at a Reynolds-number range of $50 \leqslant R_\lambda \leqslant 90$, Pumir & Shraiman (1995) and Pumir (1996) conclude

that the behaviour of the two-point correlation tensor of the vorticity suggests that as the Reynolds number increases, the small-scale properties of the flow become isotropic. However, non-zero skewness for the spanwise component of vorticity was obtained in the range of Reynolds numbers studied, suggesting that locally isotropic second-order moments may coexist with locally anisotropic higher-order moments.

Recently, an advance was made by Borue & Orszag (1996) in conducting high-Reynolds-number simulations of shear flows. They performed numerical studies of three-dimensional Kolmogorov flows at three different Reynolds numbers: Kolmogorov flow is inhomogeneous, anisotropic and highly intermittent at large scales. By using hyperviscous dissipation instead of Newtonian dissipation, they could increase the effective Reynolds numbers in their simulations. For the maximum resolution of 256^3, $R_\lambda \approx 1000$ was obtained, an order of magnitude larger than the Reynolds numbers of previous simulations of shear flows (see the references therein for the other studies where hyperviscosity is used in the numerical simulations). They confirmed Pumir's result and find non-zero skewness for the spanwise component of vorticity at numerical resolutions of 64^3 and 128^3; however, it can be seen that at those two resolutions, the components of the one-dimensional spectra did not achieve local isotropy. They also obtain results similar to our earlier study (I) of a turbulent boundary layer, and show that the small scales become locally isotropic at the highest Reynolds number (resolution 256^3) of their simulation (these results will be discussed in more detail in §3).

Therefore, to date a fairly clear picture has emerged: that is, almost all the above investigations agree with the results of our earlier study and show that in simple shear flows as the Reynolds number increases – at the least – the statistics of the second-order moments tend towards Kolmogorov's local-isotropy predictions.

The effects of extra mean strain rates on the large-scale structure of shear flows have been investigated extensively (for excellent reviews see Bradshaw 1973; Smits & Wood 1985; Purtell 1992). These extra mean rates of strain produce large nonlinear effects on the large-scale turbulence structure. The dimensionless parameter which defines the strength of an extra mean-strain rate, e, was identified by Bradshaw to be $e/(\partial U/\partial y)$, and to satisfy the thin-shear-layer assumption, $0.01 \leqslant e/(\partial U/\partial y) \leqslant 0.1$. However, as pointed out in I, the unanswered question is: will our criteria for the existence of local isotropy in simple shear flows also hold for 'complex' non-equilibrium flows at high Reynolds numbers? It is imperative that we find an answer to the above question because of the significant practical importance of complex flows. Therefore, our second set of experiments was designed to address the above question, and the results of these investigations are reported in the current paper. Our primary objective is to investigate the small-scale behaviour in distorted turbulent boundary layers at different Reynolds numbers, and our experiments adhere to all the requirements listed in §1.3 of I.

To satisfy the above objective, one possible experiment was to study the plane-of-symmetry flow upstream of an obstacle placed vertically in a fully developed two-dimensional turbulent boundary layer; for example, a circular cylinder placed with its axis perpendicular to a flat plate. A schematic diagram of this flow is shown in figure 1. Since this flow configuration has practical importance for understanding the flow physics in the vicinity of a wing–body junction of an aircraft, there have been a number of experimental investigations dealing with the large-scale structural changes that occur in this flow (Johnston 1960; Hornung & Joubert 1963; Belik 1973; Mehta 1984; Devenport & Simpson 1990 and the references therein; Smith *et al.* 1991, to name a few). In this type of boundary layer, the pressure rises strongly

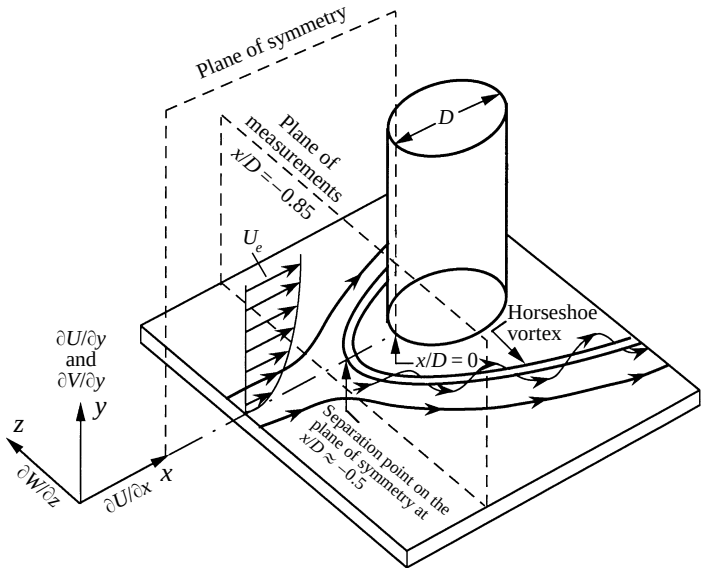

FIGURE 1. A schematic diagram of flow pattern in front of a circular cylinder placed vertically in a boundary layer: The extra mean-strain rates associated with this flow, and the plane of measurements for the present investigations, are also indicated.

as the obstacle is approached and in and near the plane of symmetry of the flow the boundary layer is also influenced by the effects of streamline (or lateral) divergence (Saddoughi & Joubert 1991). Hence in addition to the basic shear, $\partial U/\partial y$, the extra mean strain rates involved in the flow are $\partial U/\partial x$, $\partial V/\partial y$ and $\partial W/\partial z$: in the plane of symmetry, $\partial V/\partial x$ can be assumed to be very small (see for example Devenport & Simpson 1990).

To obtain the desired effects, both the height and the diameter of this cylinder should be at least of the order of the thickness of the boundary layer. Since in our study the approaching boundary-layer thickness was approximately 1.1 m, our test cylinder had the following dimensions: $D = 1.22$ m and height $L = 1.83$ m, and this large cylinder had to be fixed to the ceiling of the wind tunnel. This involved significant construction difficulties, which are discussed in the following section. The large-scale and small-scale results were taken upstream of this cylinder at the highest and the lowest (steady mean flow) possible speeds of the 80 ft $\times$ 120 ft wind tunnel.

During all of our complex-flow measurements the tunnel runs were dedicated to our experiments: however, as shown in figure 2, a full-scale F-18 fighter aircraft (wing span $\approx$ 11.5 m, length $\approx$ 16.5 m) set at an angle of attack of 50° was present in the central region of the working section for both our high- and low-speed measurements. NASA engineers estimate that the wind-tunnel flow blockage due to the aircraft at this angle of attack is approximately 8%. To identify the effects of the aircraft on the flow characteristics upstream of the cylinder, the measurements were repeated when the wind tunnel was empty. It will be seen later that the presence of the aircraft in the wind tunnel usefully increased the magnitude of mean strain rates upstream of the cylinder. Therefore, our complex-flow experiments are divided into two cases: boundary layers under the influence of (i) large and (ii) small extra mean strain rates, which correspond respectively to measurements (i) with and (ii) without the F-18 in the wind tunnel. These two flow cases are described here (see also Saddoughi 1994, 1995).

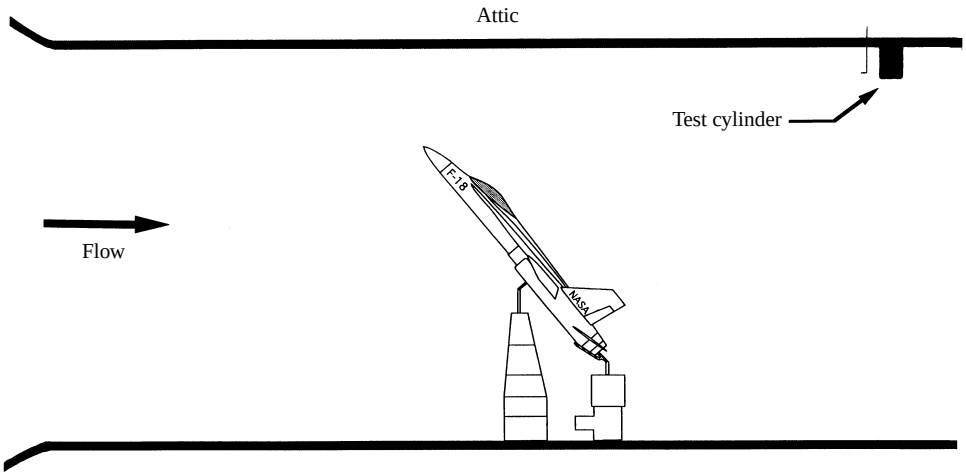

FIGURE 2. Large-extra-mean-strain-rate experiments: the relative position of the test cylinder with respect to the full-scale F-18 fighter aircraft, set at an angle of attack $\alpha \approx 50^\circ$ in the central region of the 80 ft $\times$ 120 ft wind tunnel, is shown. Drawing is to scale.

We again note that (see I) in experimental work it is only possible to concentrate on a few measures of isotropy, and undoubtedly some are satisfied before others. Therefore, we cannot be certain whether a state of *full* local isotropy is obtained.

2. Experimental facilities and techniques

The experiments described here, as in I, were conducted in the boundary layer on the test-section ceiling of the 80×120 ft wind tunnel at the Full-Scale Aerodynamics Facility at NASA Ames Research Center. The measurement station for the current experiments, was close to the location where measurements were taken in I. The only way to attach an obstacle to the ceiling of the wind tunnel was to use one of the existing light ports. Since the diameter of our test cylinder was larger than the clear opening of a typical light port, we had to use two concentric cylinders.

As shown in figure 3, the outer (test) cylinder is a ready-made light-weight Polyethylene tank (wall thickness $= \frac{1}{4}$ in., diameter $D = 4$ ft and height $L = 6$ ft) and the inner (support) cylinder is a $\frac{1}{2}$ in. thick, 8 in. diameter aluminium (6061-T651) tube, which extends for about 6 ft into the attic of the wind tunnel through the light port. A $\frac{1}{4}$ in. thick high-density Polyethylene plate and a $\frac{1}{8}$ in. thick aluminium plate are bolted respectively to the inside and outside of the bottom of the Polyethylene tank. The effective wall thickness at the bottom of the tank is $\frac{5}{8}$ in. Another $\frac{1}{4}$ in. thick high-density Polyethylene plate is bolted to the top of the tank. Steel rods are bolted to the aluminium cylinder and the space between the cylinder and the tank is filled with high-density Polyurethane foam. This provided us with a fairly light-weight (250 kg) solid cylinder. From the attic above the test-section ceiling, the support cylinder was pulled up through the light port and was attached to the attic structures. The NASA safety requirements were satisfied, and the cylinder and its attachments were designed for the maximum possible aerodynamic load, and also for dynamic loading due to seismic activity, with an overall factor of safety of 5 on yield strength.

Another light port upstream of the cylinder was used for traversing the probe through the boundary layer in the plane of symmetry. These geometrical constraints

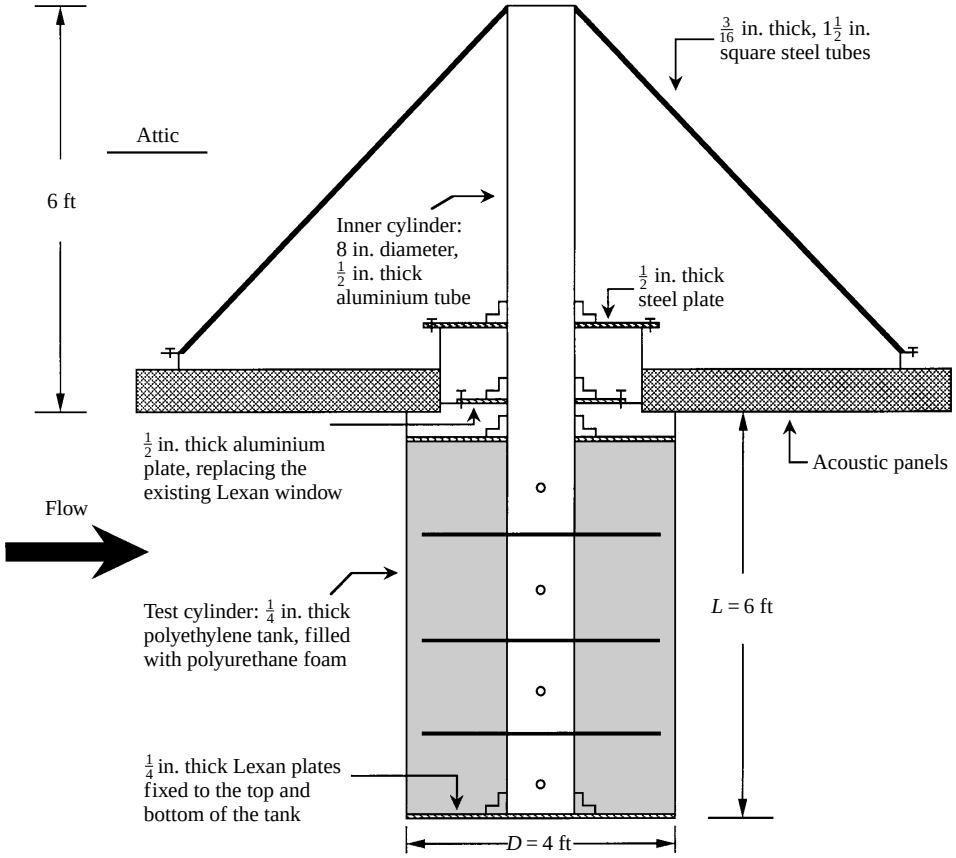

FIGURE 3. Sideview cut through the test cylinder and its support system as attached to the ceiling of the 80 ft × 120 ft wind tunnel through a light port. Drawing is not to scale.

fixed our measurement location at $x/D \approx -0.85$ with respect to the front surface of the cylinder. Therefore, as shown in figure 1, our measurement station was located upstream of the well-known separation region, which starts at $x/D \approx -0.5$. At the same longitudinal measurement station ($x/D \approx -0.85$), we have also taken flow yaw-angle measurements at two spanwise locations. These flow angles were measured with a three-tube Conrad probe operated in null reading mode.

The measurement conditions, strategy, instrumentation and procedure were all the same as those explained in §2.1 and in §2.2 of I, and will not be repeated here. Also, as in I, for the high-speed measurements, we were faced with the f^2-noise limitation of hot-wire anemometry at high frequencies. We recently presented the details of these investigations (Saddoughi & Veeravalli 1996); but we are aware that nearly three decades ago this problem was first investigated by Freymuth (1968). Unfortunately, this limitation still hampers accurate measurements at high frequencies.

3. Results and discussion

In this section the data for our high- and low-speed measurements are presented in two parts: (i) with the F-18 aircraft present in the working section and (ii) when the working section was empty. These two cases are referred to as the 'large' and

'small' extra-mean-strain-rate experiments respectively. In each part, the experimental results are divided into 'large-scale' and 'small-scale' data. Mean-flow velocity and Reynolds-stress profiles, as well as the large-scale flatness factors are analysed, as in I, to determine the large-scale characteristics and obtain the parameters governing the development of the boundary layer. Effects of the distortion of the large eddies were identified by comparing these profiles with the results from our plane turbulent boundary-layer study (I). These large-scale results facilitated the choice of points at which the small-scale measurements were taken.

3.1. *Distorted boundary layers: Large-extra-mean-strain-rate experiments*

3.1.1. *Analysis of large-scale data*

The high-speed and low-speed measurements to be discussed here correspond to the wind-tunnel reference velocities of $U_{ref} \approx 51.25$ and 10.75 m s^{-1} respectively (measured near the start of the working section). Figure 4 shows the mean-flow data: in this, and all subsequent figures where profiles of large-scale parameters are presented, the vertical arrows on the abscissa indicate y-positions at which small-scale measurements were taken (see §3.1.2).

In figure 4(a), the normalized profiles of the longitudinal mean velocity, U/U_{ref}, obtained in I for both high- and low-speed cases are compared with the profiles for the present distorted boundary layers. The solid line on the present data corresponds to the least-squares polynomial fit to the high-speed results, which has been used to obtain the mean-flow integral parameters for these experiments. The shape of the velocity profile for the distorted boundary layer is typical of flows with large adverse pressure gradients: note the flattening of the profile in the middle of the layer.

The boundary-layer thickness, δ, has increased compared to I, and is approximately 1350 mm in the distorted boundary layer. Here, the momentum thickness θ and the shape factor H are approximately 168 mm and 1.8 respectively. The maximum Reynolds number based on momentum thickness is $R_\theta \approx 510\,000$, which is the largest ever attained in laboratory boundary-layer flows. It is also instructive to note that the maximum R_θ of the present complex-flow experiments is of the same order as those obtained in flight on a typical commercial aircraft, a nuclear submarine ($R_\theta \approx 300\,000$), or the space shuttle ($R_\theta \approx 430\,000$) (Gad-el-Hak & Bandyopadhyay 1994). All the integral parameters for the present experiments are given in table 1.

Figure 4(b) shows the normalized profiles of the vertical velocity component, V/U_{ref}. A least-squares polynomial fit to the V profile (the solid line) was used to obtain the values of $\partial V/\partial y$. The magnitudes of the extra-mean-strain rate due to the streamline divergence, $\partial W/\partial z$, influencing the plane of symmetry of the flow can be obtained from $(\partial W/\partial z) = U(\partial\beta/\partial z)$ (see for example Saddoughi & Joubert 1991), where β is the flow yaw angle measured at different spanwise locations z. The profiles of β measured by our yaw-meter Conrad probe for three spanwise locations ($z/D = -0.21$, 0, and 0.21) through the boundary layers are shown in figure 4(c). It can be seen that, as expected in the plane of symmetry, the crossflow W is approximately equal to zero. The profiles at the spanwise locations are typical of three-dimensional boundary layers: larger flow yaw angles near the wall than in the outer part of the boundary layer. Finally, the continuity equation was used to obtain the $\partial U/\partial x$ values.

The profiles of all these extra-mean-strain rates are shown in figure 5, where they are compared with the profiles of the basic shear $\partial U/\partial y$ for both the plane-flow (I) and distorted boundary layers. It can be seen from this figure that, as expected (Bradshaw 1973; Smits & Wood 1985), the extra-mean-strain rates mostly affect the outer layer

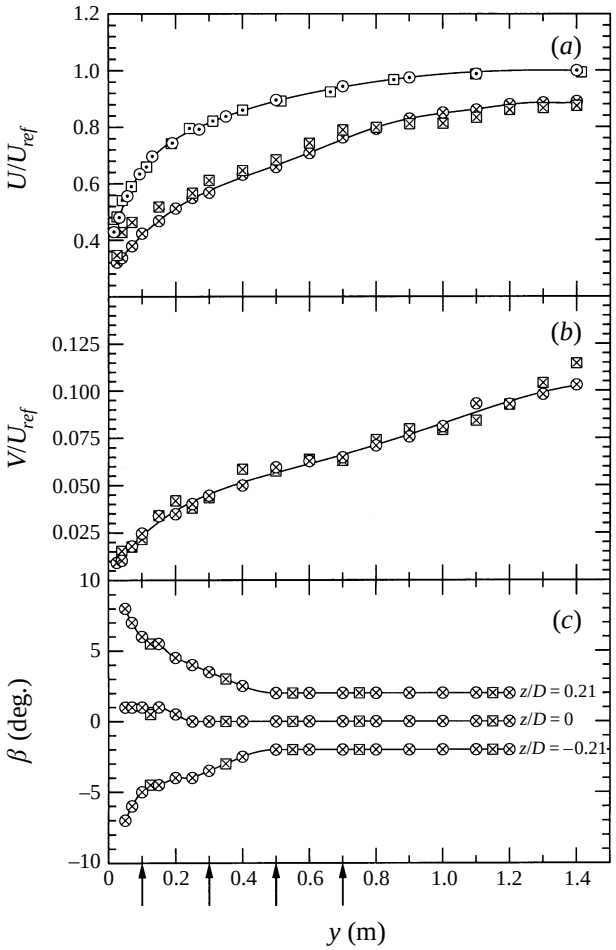

FIGURE 4. Mean-flow data measured at two different free-stream velocities. (*a*) Normalized longitudinal mean-velocity profiles, U/U_{ref}, measured in plane (I) and large-extra-mean-strain rate boundary layers. (*b*) Normalized vertical mean-velocity profiles, V/U_{ref}, and (*c*) flow yaw-angle profiles, β at different spanwise locations, measured in large-extra-mean-strain rate boundary layers. ⊙, $U_{ref} \approx 50$ m s^{-1} ($R_\theta \approx 370\,000$) and ⊡, $U_{ref} \approx 10$ m s^{-1} $R_\theta \approx 74\,000$) from I; ⊗, $U_{ref} \approx 51.25$ m s^{-1} $R_\theta \approx 510\,000$) and ⊠, $U_{ref} \approx 10.75$ m s^{-1} ($R_\theta \approx 107\,000$) large-extra-mean-strain rate boundary layers. Lines are the least-squares polynomial fits to the data for each case. Vertical arrows on the abscissa indicate y-positions for small-scale measurements in distorted boundary layers.

(here 300 mm $\leqslant y \leqslant$ 800 mm or $0.2 \leqslant y/\delta \leqslant 0.6$) of the boundary layer. This figure also shows that typical absolute values of $(\partial V/\partial y)/(\partial U/\partial y)$, $(\partial W/\partial z)/(\partial U/\partial y)$, and $(\partial U/\partial x)/(\partial U/\partial y)$ are larger than 0.1, 0.2 and 0.3 respectively. These are very large values for extra-mean-strain rates and they produce large nonlinear effects on the large-scale structures of the boundary layers (Bradshaw 1973). The values of these parameters at the y-positions where small-scale measurements were obtained are given in table 1. The intensity (or rapidity) of a mean-strain rate can be characterized by $s = (s_{ij}s_{ij}/2)^{1/2}$, (see for example Lee & Reynolds 1985; Saddoughi 1993). For the present experiments, $s = ([(\partial U/\partial y)^2/2 + (\partial U/\partial x)^2 + (\partial V/\partial y)^2 + (\partial W/\partial z)^2]/2)^{1/2}$, and to be consistent with our definition in I, we shall use $S = 2s$ as the equivalent mean-strain rate.

Case	Low speed				High speed		
U_{ref} (m s^{-1})	10.75				51.5		
δ (mm)	1350				1350		
δ^* (mm)	298				298		
θ (mm)	168				168		
C_f	0.00078				0.00078		
U_τ (m s^{-1})	0.186				0.89		
R_θ	107 000				510 000		
y (mm)	100	300	500	700	100	300	500
y^+	1250	3750	6250	8750	6000	18 000	30 000
U (m s^{-1})	5.9	7.0	7.4	8.9	22.4	29.6	34.6
$\partial U/\partial y$ (s^{-1})	12.9	5.6	4.6	5.0	62.0	27.0	22.0
$-\partial U/\partial x$ (s^{-1})	3.5	2.3	1.5	1.7	16.9	10.8	7.2
$\partial V/\partial y$ (s^{-1})	1.8	0.8	0.5	0.5	8.4	3.7	2.5
$\partial W/\partial z$ (s^{-1})	1.8	1.5	1.0	1.1	8.5	7.1	4.8
S (s^{-1})	14.3	6.9	5.3	5.8	68.5	33.0	25.2
$\overline{u_1^2}$ (m^2 s^{-2})	1.23	0.73	0.60	0.29	32.1	23.6	17.8
$\overline{u_2^2}$ (m^2 s^{-2})	0.34	0.36	0.33	0.20	7.3	8.7	7.2
$\overline{u_3^2}$ (m^2 s^{-2})	0.60	0.47	0.44	0.23	13.3	11.9	10.2
$-\overline{u_1 u_2}$ (m^2 s^{-2})	0.12	0.19	0.17	0.15	3.0	4.3	3.5
$(\overline{u_1^2})^{1/2}/U$	0.20	0.13	0.11	0.06	0.25	0.16	0.12
q^2 (m^2 s^{-2})	2.17	1.56	1.37	0.72	52.7	44.2	35.2
ε (m^2 s^{-3})	2.18	0.82	0.53	0.19	280	144	92
η (mm)	0.2	0.25	0.28	0.37	0.06	0.07	0.08
Spatial resolution	2.5η	2η	1.8η	1.3η	8.5η	7η	6.5η
f_η (kHz)	4.6	4.4	4.2	3.9	60	68	70
R_λ	830	810	820	670	1960	1950	1850
S^*	14.2	13.0	13.7	22.0	13.0	10.0	9.6
S_c^*	0.038	0.03	0.028	0.052	0.015	0.011	0.01

TABLE 1. Flow parameters for the large-extra-mean-strain-rate experiments

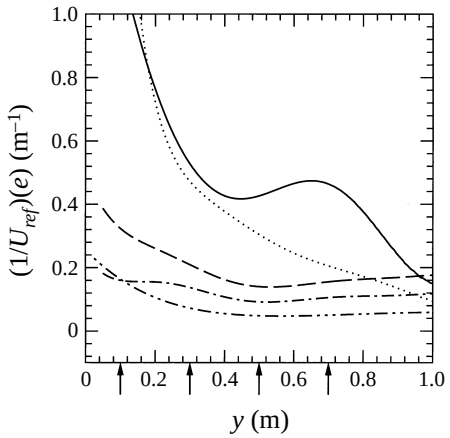

FIGURE 5. Profiles of extra mean-strain rates, e, compared with basic shear, $\partial U/\partial y$. ……, $\partial U/\partial y$ for plane boundary layer of I. ———, $\partial U/\partial y$; - - - - -, $-\partial U/\partial x$; –·–, $\partial W/\partial z$; –··–, $\partial V/\partial y$ for the present distorted boundary layer. Arrows as figure 4.

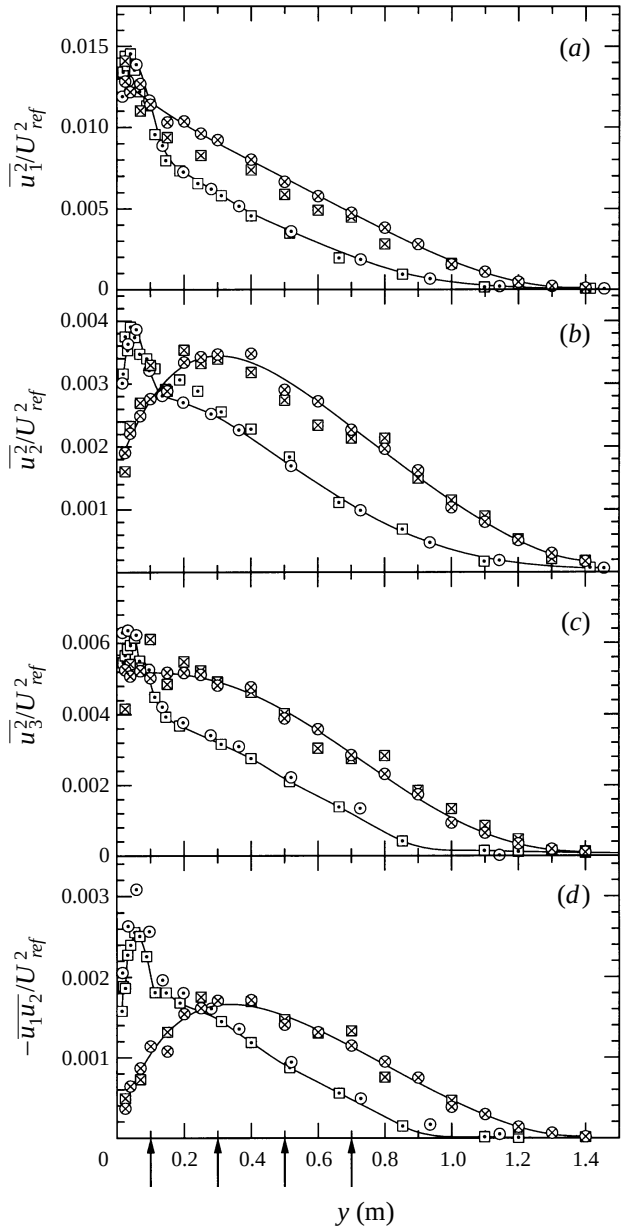

FIGURE 6. Profiles of Reynolds stresses measured in plane (I) and large-extra-mean-strain-rate boundary layers at low and high free-stream velocities: (*a*) $\overline{u_1^2}/U_{ref}^2$, (*b*) $\overline{u_2^2}/U_{ref}^2$, (*c*) $\overline{u_3^2}/U_{ref}^2$, (*d*) $-\overline{u_1 u_2}/U_{ref}^2$. For key to symbols see figure 4.

The profiles of the Reynolds normal stresses ($\overline{u_1^2}/U_{ref}^2, \overline{u_2^2}/U_{ref}^2, \overline{u_3^2}/U_{ref}^2$) and shear stress $-\overline{u_1 u_2}/U_{ref}^2$ for the distorted boundary layers at high and low speeds are compared with the profiles for the plane-boundary layers (I) in figure 6. The profiles for the distorted boundary layers are quite different from those in the plane flow. The peaks of $\overline{u_2^2}$ and the shear stress, $-\overline{u_1 u_2}$, profiles have moved away from the wall to $y \approx 300$ mm, and in the outer part of the layer the values of all the Reynolds stresses have increased, due to the combined effects of adverse pressure gradient and streamline divergence.

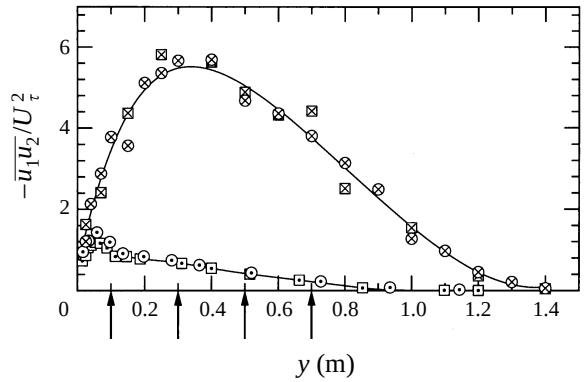

FIGURE 7. Scaling of the Reynolds shear-stress profiles (figure 6*d*) using U_τ as velocity scale. For key to symbols see figure 4.

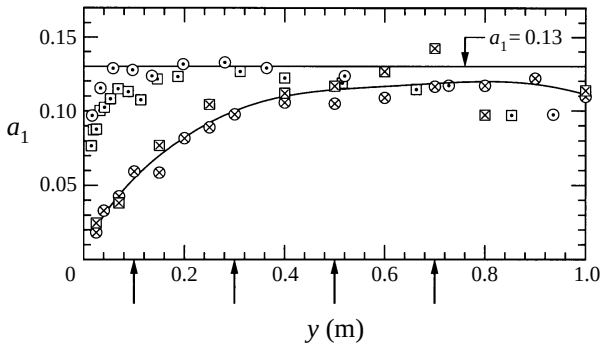

FIGURE 8. The structure parameter, $a_1 \equiv -\overline{u_1u_2}/q^2$. The canonical smooth-wall value, $a_1 = 0.13$ (Townsend 1976), is also shown. For key to symbols see figure 4.

From figure 6(*d*) it can be deduced that at the wall $\tau/\rho U_{ref}^2 \approx 0.0003$, and from figure 4(*a*) that the free stream $U/U_{ref} \approx 0.88$. Based on these values the friction coefficient $C_f \approx 0.00078$ is obtained, corresponding to shear velocities $U_\tau \approx 0.89$ and 0.186 m s^{-1} for the high- and low-speed cases respectively. It is important to note that, as in I, the U_τ values are used only to estimate the values of y^+ and as a scaling parameter when our large-scale mean results are compared with those for other boundary layers: for example, we have used U_τ as the scaling velocity to replot the Reynolds shear-stress profiles in figure 7. As far as the scaling of the small-scale data is concerned, the friction velocity will not play any role – the only relevant mean-flow parameter is S, which, as shown earlier, is obtained by differentiating the least-square polynomial fits presented in figure 4.

However, the changes in the large-scale structure of the turbulence can be seen in figure 8, which shows the profiles of Townsend's (1976) structure parameter, $a_1 \equiv (-\overline{u_1u_2}/q^2)$, where q^2 ($\equiv \overline{u_iu_i}$) is twice the turbulent kinetic energy per unit mass. The very low values of this parameter in the inner part of the boundary layer and their recovery to the canonical values in the outer part of the layer are due to the effects of large adverse pressure gradients (see Bradshaw 1967).

The flatness factor of the velocity fluctuations is defined as $F_{u_i} \equiv \overline{u_i^4}/(\overline{u_i^2})^2$, where $i = 1$, 2 or 3 is a measure of the width of the distribution about the mean, and for a Gaussian process $F = 3$. It is known that in the inner half of two-dimensional

zero-pressure-gradient turbulent boundary layers approximately Gaussian values for flatness factors are obtained. In the outer half of the boundary layer the F_{u_i} values increase due to the large-scale intermittency and reach their maxima near the edge of the boundary layer (see for example Klebanoff 1954). Extra mean-strain rates affect the large-scale intermittency in the outer part of the boundary layers (for a review see Saddoughi 1989): for example, lateral divergence results in an increase in the extent of the intermittent region, but adverse pressure gradient apparently has the opposite effect (Head & Patel 1968; Saddoughi & Joubert 1991). However, Simpson, Chew & Shivaprasad (1981) concluded that in the log layer and the outer layer of boundary layers, adverse pressure gradients do not have much effect on the flatness factor.

The profiles of the flatness factors in the present distorted boundary layers, for both the low- and high-speed cases, are compared with the profiles for the plane-flow case in figure 9. The flatness $F_{u_i} \approx 3$ in the inner half of the boundary layer, which includes all four y-positions where small-scale measurements (see §3.1.2) were taken. Recall that the boundary-layer thicknesses at the centreline measurement station for the plane and distorted boundary layers were 1.1 and 1.35 m respectively. The maxima in the F_{u_i} profiles for both cases are located near the boundary-layer edges, but the peaks in the distorted boundary layers are much larger. The large-scale skewness $S_{u_i} \equiv \overline{u_i^3}/(\overline{u_i^2})^{3/2}$ profiles (not shown) exhibited similar increases in the maximum (absolute) magnitudes of S_{u_1} and S_{u_2} in the distorted boundary layers (in a two-dimensional mean flow such as the plane-of-symmetry flow of the present experiments S_{u_3} is nominally zero, see for example Shiloh, Shivaprasad & Simpson 1981). Overall, these results tend to show that the fluctuating signals near the edge of the distorted boundary layers (with the F-18 present in the wind tunnel) are more intermittent and have sharper spikes than those in the plane boundary layer (I).

3.1.2. *Analysis of small-scale data*

In this section, the small-scale measurements of the three components of velocity made for (i) high-speed and (ii) low-speed cases are presented. These measurements were taken at $y = 100$, 300 and 500 mm. Recall that in I, measurements were presented for only two locations, which were called the inner-layer and mid-layer positions. For the present investigations the $y = 100$ mm position is still considered to be located in the inner layer of the boundary layer, since $y/\delta \approx 0.074$, and $y^+ \approx 1250$ and 6000 for the low-speed and high-speed cases respectively. The $y = 300$ mm position was chosen because the peak of the Reynolds stresses occurred there, and we chose the $y = 500$ mm position, because it represents the mid-layer position in I. To investigate a slight deviation from the local-isotropy predictions that occurred only at the outer-layer positions in the low-speed case, measurements were also taken at $y = 700$ mm. The measurement locations $y = 100$, 300, 500 and 700 mm will be referred to hereafter as the inner-layer, maximum-stress, mid-layer and outer-layer positions respectively. The relevant flow parameters at these positions, for both free-stream velocities, are given in table 1.

The local turbulence intensities, defined as the r.m.s. longitudinal velocity fluctuations normalized by the local mean velocities, $(\overline{u_1^2})^{1/2}/U$, at $y = 100$, 300, 500 and 700 mm are approximately equal to 25%, 15%, 12% and 8% respectively. As discussed in I we use Taylor's (1935) hypothesis to deduce wavenumber spectra from frequency spectra. The errors arising from the use of Taylor's hypothesis can be calculated using the equations given by Wyngaard & Clifford (1977), which are based on an extension of Lumley's (1965) work. The necessary corrections are given as

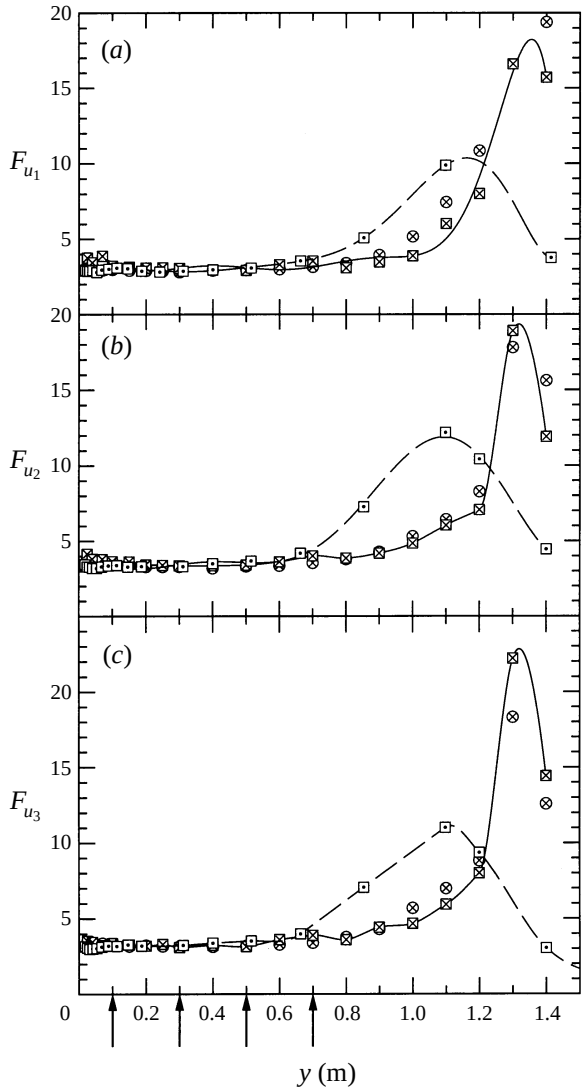

FIGURE 9. Profiles of large-scale flatness factors, $F_{u_i} \equiv \overline{u_i^4}/(\overline{u_i^2})^2$. (*a*) u_1-component, (*b*) u_2-component, (*c*) u_3-component. For key to symbols see figure 4.

equations (20)–(23) in I. The maximum error occurs in the dissipation range, and for the above four measurement locations, the largest errors (which are in the measurements of the transverse components) are approximately equal to 15%, 8%, 5% and 2% respectively. However, these errors are reduced in the inertial subrange to less than 5%, 2%, 1% and 1% respectively.

For the current experiments, the Kolmogorov frequency, $f_\eta \equiv U/(2\pi\eta)$, where η was calculated by using the isotropic relation for the dissipation (see I), changed from approximately 70 kHz in the high-speed measurements to 3.9 kHz in the low-speed measurements (see table 1 for all the values). Because of the f^2 behaviour of the electronic noise at the tail of the spectrum, and also due to lack of sufficient hot-wire spatial resolution, the dissipation range, as in I, could not be resolved for the high-speed case. However, the high-speed results remain very important for the

investigation of inertial-subrange scaling because they are at a much higher R_λ, and in this case the measurements are fairly accurate since the errors arising from failure of Taylor's hypothesis are very small.

For the low-speed case, measurements were obtained with no contamination from electronics noise. At the inner-layer position, due to the lack of hot-wire spatial resolution and fairly large errors arising from Taylor's hypothesis in the dissipation range, we can trust our measurements only up to $k_1\eta \approx 0.45$. However, hot-wire resolution and Taylor's hypothesis improve as one moves away from the wall (see table 1), and at the outer-layer position ($y = 700$ mm) our best spatial resolution (1.3η) is achieved.

Figure 10 is similar to figure 9 of I, and shows Kolmogorov's universal scaling of the longitudinal power spectra (I, equations (3) and (7)) of previous experimental work taken from Chapman (1979), with later additions. As an example of the spectral measurements in the current investigations, we have added two spectra to this figure. The data added were taken at $R_\lambda \approx 2000$ and 850 in the high-speed and low-speed cases respectively. Note that the extent of the $-\frac{5}{3}$ range increases with Reynolds number. The present complex turbulent boundary-layer measurements agree very well with the previous data.

In the following we first discuss the high-speed measurements and then proceed to analyse the low-speed data. The microscale Reynolds numbers for the measured spectra in the high-speed and low-speed sets are of the order of 2000 and 800 respectively. Therefore, one can consider that the two sets represent data taken at high and low Reynolds numbers. Hence, comparisons of data within each set and between the two sets show the effects of different mean shear and Reynolds number respectively.

(i) *High-speed experiments*

We first examine Kolmogorov's inertial-subrange scaling laws for spectra (I, equations (7) and (8)) and structure functions (I, equations (12)–(14)). This is followed by an investigation of the shear-stress cospectra (I, equations (10) and (30)). Finally, a consistency test (I, equation (4)) is applied to verify the local-isotropy hypothesis more directly.

To confirm the inertial-subrange power laws (I, (7) and (8)), we form 'compensated' spectra $\varepsilon^{-2/3}k_1^{5/3}E_{\alpha\alpha}(k_1)$, where $\alpha = 1$, 2 or 3 (no summation over α). In the inertial subrange, these should be independent of wavenumber and equal to the Kolmogorov constants for one-dimensional spectra. In figure 11 the compensated longitudinal (u_1) spectra measured at the three different (inner-layer, maximum-stress and mid-layer) measurement positions are plotted against $k_1\eta$. The compensated ninth-order, least-square polynomial log-log fits of $E_{11}(k_1)$ are also included there. As explained in I, for the high-speed data a good direct estimate for dissipation is not available, and we have used the method described in I to calculate it. Briefly, this method involves (i) plotting $k_1^{5/3}E_{11}(k_1)$ versus k_1 (not shown here) and (ii) using equation (7) of I in the inertial subrange, which indicates that the flat region should be equal to $C_1\varepsilon^{2/3}$. Since our previous data (I) indicated that $C = 1.5 \pm 0.1$ (where $C_1 = \frac{18}{55}C$), we used this value and the above plots to calculate $\varepsilon \approx 280$, 144 and 92 $\mathrm{m^2s^{-3}}$ at the measurement positions $y = 100$, 300 and 500 mm respectively.

It can be seen from figure 11 that at this high R_λ the compensated u_1-spectra exhibit more than one decade of $-\frac{5}{3}$ range, but less than the log-log plot (figure 10) suggested. Figures 12 and 13 show the compensated u_2- and u_3-spectra respectively

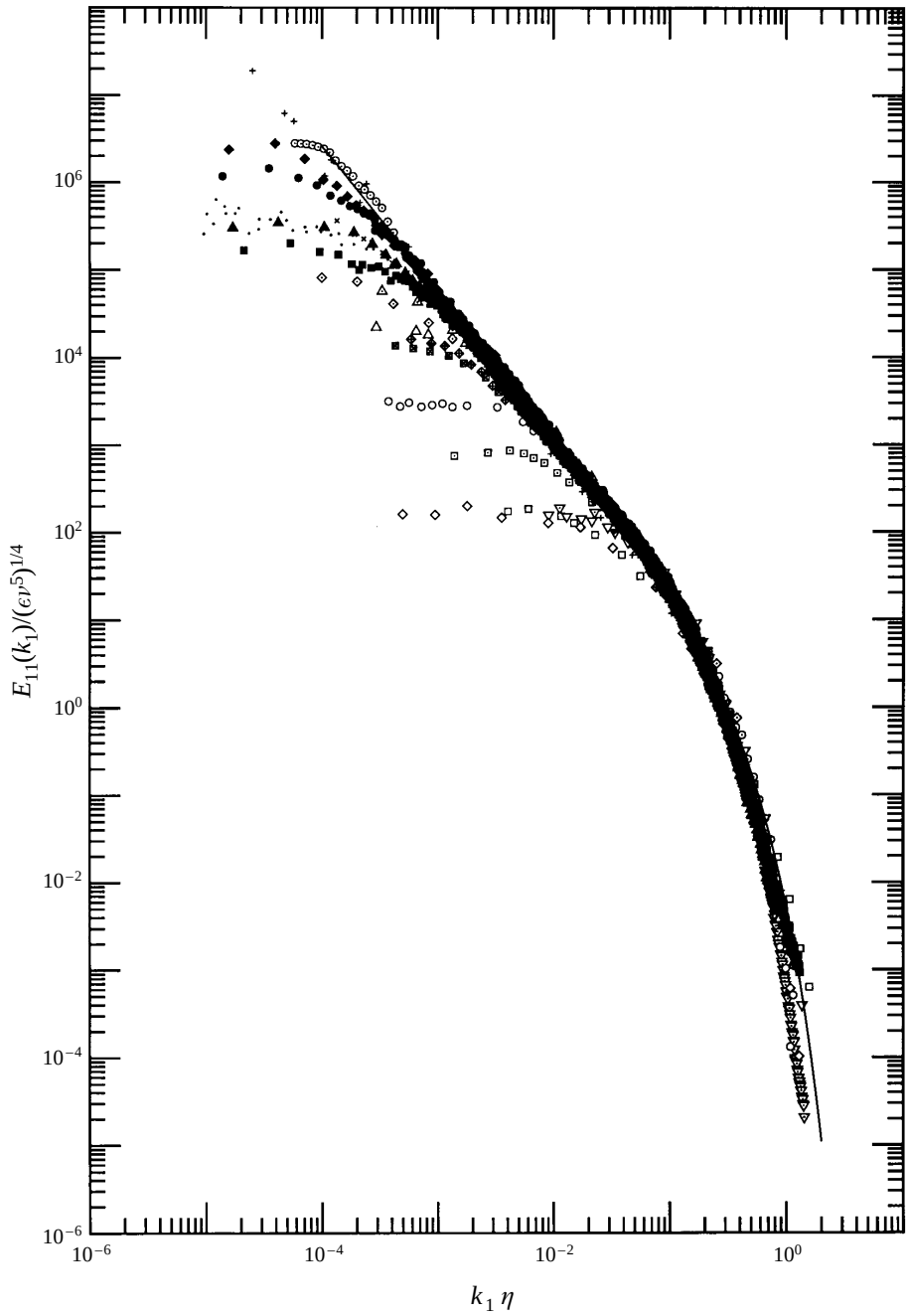

FIGURE 10. Kolmogorov's universal scaling for one-dimensional longitudinal power spectra. This is figure 9 of I, which is a compilation from Chapman (1979), with later additions. The present spectra for the large-extra-mean-strain rate boundary layers at high-speed (◆, $U_{ref} \approx 51.25$ m s^{-1}, $R_\lambda \approx 2000$) and low-speed (▲, $U_{ref} \approx 10.75$ m s^{-1}, $R_\lambda \approx 850$) cases are compared with data from other experiments. For key to other symbols see figure 9 of I.

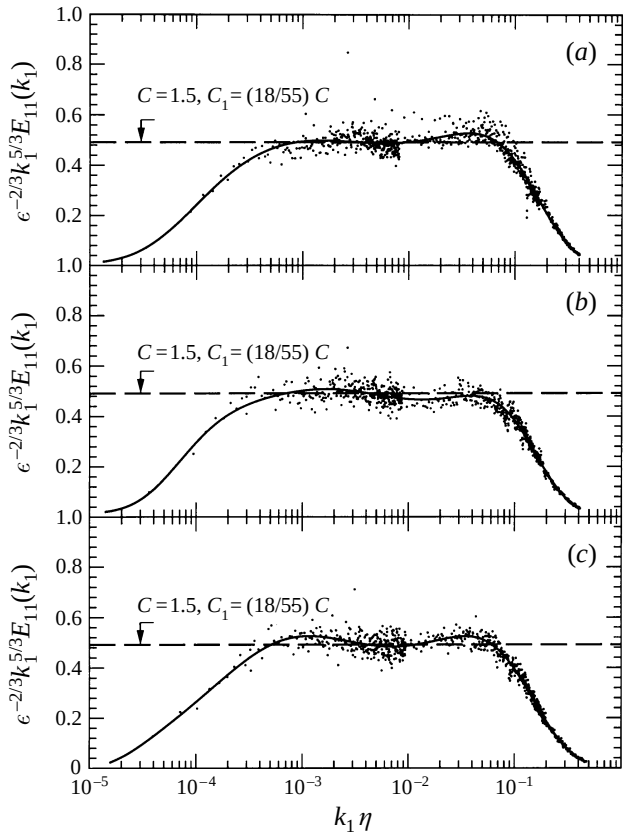

FIGURE 11. Compensated longitudinal (u_1) spectra measured at different locations in the large-extra-mean-strain-rate boundary layer for the high-speed case. (*a*) Mid-layer position ($y = 500$ mm, $y^+ \approx 30\,000$, $R_\lambda \approx 1850$). (*b*) Maximum-stress position ($y = 300$ mm, $y^+ \approx 18\,000$, $R_\lambda \approx 1950$). (*c*) Inner-layer position ($y = 100$ mm, $y^+ \approx 6000$, $R_\lambda \approx 1960$). Only the data for wavenumber range $k_1\eta < 0.15$ can be accepted. Solid lines are the ninth-order, least-square, log-log polynomial fits to the spectral data.

for the high-speed case. These transverse spectra contain well-defined $-\frac{5}{3}$ ranges and are, as expected, equal to each other and larger than the u_1-spectrum by the $\frac{4}{3}$ factor. Since the microscale Reynolds numbers are approximately the same at the three measurement locations in each figure, one can see the effects of the different mean shears. For example in figure 12(*c*), the u_2-spectrum measured at the inner-layer position at $R_\lambda \approx 2000$ does not show a perfectly flat region for the inertial subrange. However, the spectra for the outer-layer positions, which are at similar (or slightly smaller) Reynolds numbers, display more than one decade of the expected $-\frac{5}{3}$ range. This is similar to the behaviour observed in the plane-flow high-speed case. As in I (see references given therein for other investigations and also see Yakhot 1994; Falkovich 1994; Lohse & Muller-Groeling 1995; Borue & Orszag 1996), once a well-defined inertial subrange is present, all the compensated spectra have a 'bump' between the inertial subrange and the dissipation range.

The structure functions, given by equations (12), (13) and (14) of I, were checked for consistency with Kolmogorov's inertial-range scaling laws. As in I, plots of the third-order structure function for the longitudinal velocity fluctuations I, equation (14),

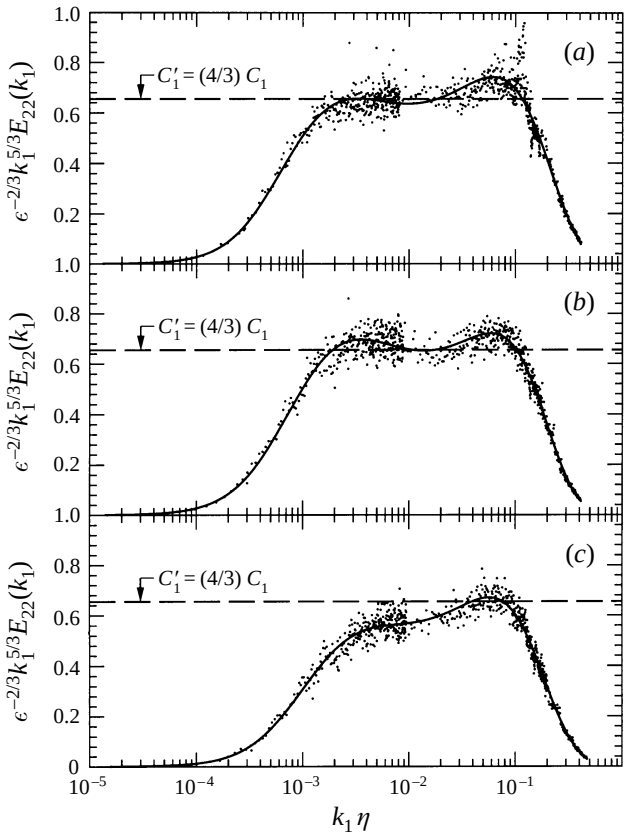

FIGURE 12. As figure 11, but compensated transverse (u_2) spectra.

were used to calculate dissipation values at the three measurement locations. These were approximately 15% lower than those estimated from the spectra. The microscale Reynolds numbers obtained using these dissipation rates were approximately 2100, 2090 and 1985 at $y = 100$, 300 and 500 mm respectively. Using these dissipation values, we investigated the behaviour of the third- and second-order structure functions at the three measurement locations.

The compensated third- and second-order structure functions, measured at the maximum-stress position ($y = 300$ mm), are shown in figures 14 and 15 respectively. The values of the separation r were calculated using Taylor's hypothesis, $r = \tau U$, where τ is the time interval and U is the local mean velocity. It is important that log-linear plots of these structure functions be inspected, rather than the customary log-log plots which tend to mask the variations that may exist in the inertial subrange. In these figures, as explained in I, there are three different data sets corresponding to the three frequency bands used to resolve the large scales, the inertial subrange, and the dissipation range. Note that figures 14 and 15 contain the actual data, not polynomial fits. The third-order structure function (figure 14) displays about two decades of relatively flat correlation.

The three components of the second-order structure functions (figure 15) exhibit inertial subranges, albeit even at this high Reynolds number the exponents appear to be slightly different from $\frac{2}{3}$; however, at the outer-layer positions (not shown) they came closer to the expected value. This behaviour was also observed in I. The

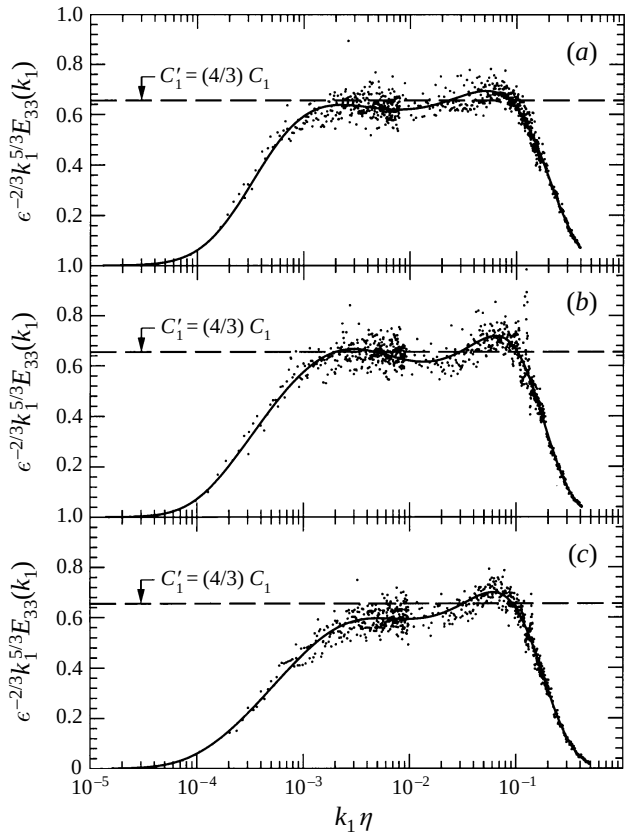

FIGURE 13. As figure 11, but compensated transverse (u_3) spectra.

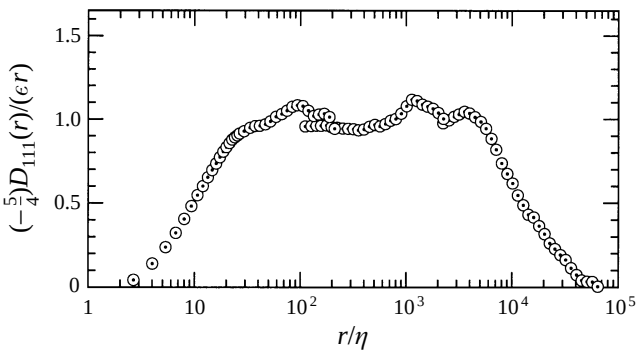

FIGURE 14. Compensated third-order structure function for longitudinal velocity fluctuations measured at the maximum-stress position in the large-extra-mean-strain-rate boundary layer for the high-speed case ($y = 300$ mm, $y^+ \approx 18\,000$, $R_\lambda \approx 2090$, based on the dissipation from the third-order structure function).

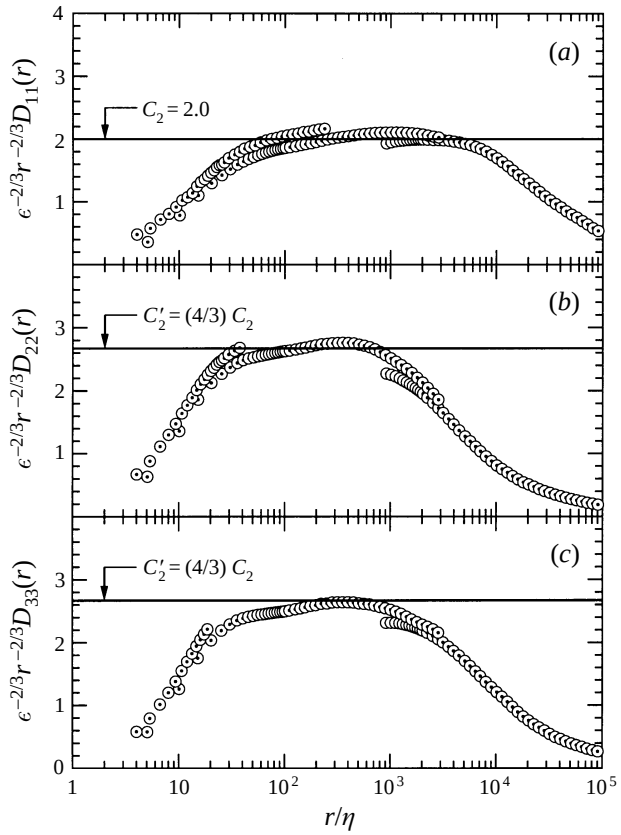

FIGURE 15. Compensated second-order structure functions for longitudinal and transverse velocity fluctuations measured at the maximum-stress position in the large-extra-mean-strain-rate boundary layer for the high-speed case ($y = 300$ mm, $y^+ \approx 18\,000$, $R_\lambda \approx 2090$, based on the dissipation from the third-order structure function). (*a*) u_1-structure function; (*b*) u_2-structure function; (*c*) u_3-structure function.

important point is that, at a given position in the boundary layer, the u_2- and u_3-structure functions in the inertial subrange were equal to each other and were larger than the u_1-structure function by the factor $\frac{4}{3}$, to within the measurement accuracy. As can be seen in figure 15, similar to I, the data agrees very well with the Kolmogorov constant $C_2 = 2.0$, which corresponds to $C = 1.5$.

The main aim of the present investigation is to study the effects of extra mean-strain rates on local isotropy. In I the parameters characterizing the effects of mean shear on turbulence were identified as $S^* \equiv Sq^2/\varepsilon$ (see for example Moin 1990) and $S_c^* \equiv S(\nu/\varepsilon)^{1/2}$ (Corrsin 1958; Uberoi 1957). Recall that we define $S \equiv 2(s_{ij}s_{ij}/2)^{1/2}$. In general, there is some degree of uncertainty associated with the experimental estimates of S^* and S_c^* because they involve gradients calculated from data points that are widely spaced and the dissipation values for the present cases are accurate to 15% at best. It is also clear that the uncertainties in these parameters are larger in the present experiments than in I, because we have more s_{ij} to evaluate. To calculate these parameters, we have used the dissipation values obtained from the spectral measurements, and the values of S obtained by the methods explained in §3.1.1. The values of these parameters are given in table 1. Note that for this high-speed (or

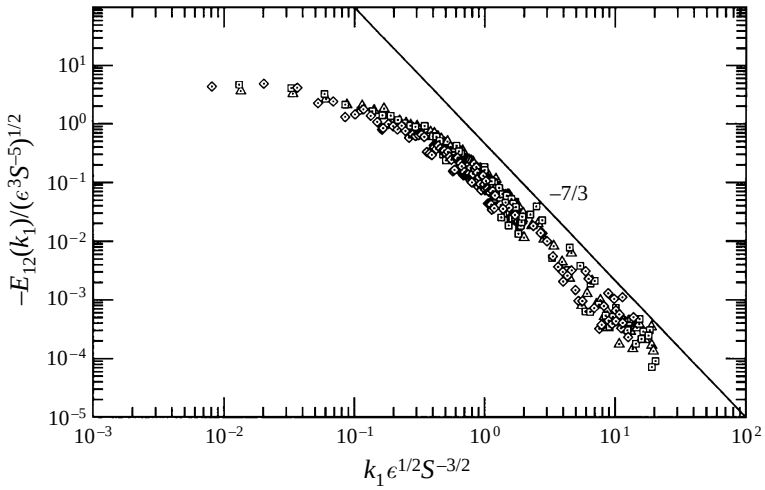

FIGURE 16. Shear-stress cospectra non-dimensionalized using $(\varepsilon/S^3)^{1/2}$ and $(\varepsilon/S)^{1/2}$ as length and velocity scales respectively, measured at different locations in the large-extra-mean-strain-rate boundary layer for the high-speed case. △, mid-layer position ($y = 500$ mm, $y^+ \approx 30\,000$, $R_\lambda \approx 1850$); ⊡, maximum-stress position ($y = 300$ mm, $y^+ \approx 18\,000$, $R_\lambda \approx 1950$); ◇, inner-layer position ($y = 100$ mm, $y^+ \approx 6000$, $R_\lambda \approx 1960$).

high-Reynolds-number) case, the values of S_c^* at all the measurement stations are of the order of 0.01. Recall from I that one decade of isotropic inertial subrange requires S_c^* of not more than about 0.01. However, in this non-equilibrium boundary layer, this condition requires a higher Reynolds number ($R_\lambda \approx 2000$) than in I ($R_\lambda \approx 1500$).

We analyse the shear-stress cospectra $E_{12}(k_1)$, the behaviour of which was described by Lumley (1967) (and recently by Yakhot 1994; Grossman *et al.* 1994; and Canuto & Dubovikov 1996*a,b*, where they obtain an analytical solution for the cospectra and compare their results with our data in I). Lumley's equation (see (30) in I) states that when k_1 is much larger than $(S^3/\varepsilon)^{1/2}$, but small compared to the Kolmogorov wavenumber, the shear-stress cospectrum should scale linearly with S. The cospectra measured at different locations in the boundary layer for the high-speed case are shown in figure 16. The collapse achieved by using $(\varepsilon/S^3)^{1/2}$ and $(\varepsilon/S)^{1/2}$ as length and velocity scales respectively is similar to I: the cospectra do apparently follow the $-\frac{7}{3}$ law and scale with S in the inertial subrange, and the $-\frac{7}{3}$ range starts at a non-dimensional wavenumber $k_1(\varepsilon/S^3)^{1/2} \approx 1$. The value of the constant C_0 (from I, (30)) for one-dimensional cospectra obtained in our plane turbulent boundary-layer case (I) was approximately 0.15, which agreed with Wyngaard & Cote (1972). In the present investigations we also estimate $C_0 \approx 0.15$. Canuto *et al.*'s (1996) numerical result predicts the value of the constant to be $\frac{145}{1729}$, and Borue & Orszag (1996) obtained $C_0 = 0.2$–0.4 in their numerical study.

The behaviour of the cospectra can also be examined in terms of the correlation-coefficient spectra $R_{12}(k_1)$ given by equation (10) in I. If the spectra involved contain well-defined inertial subranges, such that both u_1- and u_2-spectra have $-\frac{5}{3}$ ranges and the cospectrum exhibits a $-\frac{7}{3}$ power law, then the correlation-coefficient spectrum should decay towards isotropy as $k_1^{-2/3}$. In I, we found that these correlation coefficients decayed algebraically in accordance with the dynamical model of Nelkin & Nakano (1983) (see also Nelkin 1994). Borue & Orszag (1996) confirmed our results. The $R_{12}(k_1)$ spectra are shown plotted against non-dimensional wavenumber

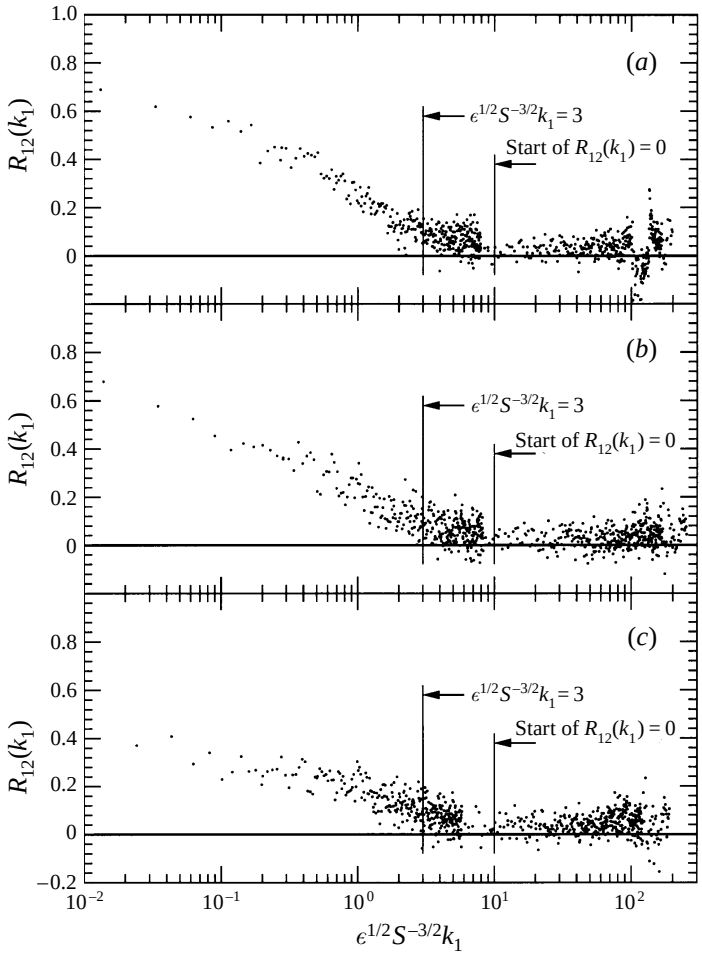

FIGURE 17. Correlation-coefficient spectra measured at different locations in the large-extra-mean-strain-rate boundary layer for the high-speed case. Wavenumber is scaled using the lengthscale $(\varepsilon/S^3)^{1/2}$. For key to captions for (*a–c*) see figure 11.

$k_1(\varepsilon/S^3)^{1/2}$ in figure 17. As in I, both positive and negative values are inferred from the measurements in the high-wavenumber ranges at all the measurement stations. This has been also observed in previous experiments and direct numerical simulations (see the references in I, and also see Borue & Orszag 1996, who obtain fairly large negative values at high wavenumbers). We see from figure 17 that for $k_1(\varepsilon/S^3)^{1/2} > 10$, $R_{12}(k_1) \approx 0$. This shows that the lower-wavenumber limit of locally-isotropic behaviour for complex shear flows at high Reynolds number is $k_1(\varepsilon/S^3)^{1/2} \approx 10$: this is the same result we obtained in I. Borue & Orszag (1996) obtained the essentially equivalent value of about 9 for this limit.

Finally, a direct test of local isotropy is to determine if the data satisfy equation (4) of I, which states that for isotropic motion, (*a*) the transverse spectra $E_{22}(k_1)$ and $E_{33}(k_1)$ are equal and (*b*) they are directly related to the longitudinal spectrum $E_{11}(k_1)$ (see for example Batchelor 1953). The ratios of the measured u_3-spectrum to u_2-spectrum, $E_{33}^{meas}(k_1)/E_{22}^{meas}(k_1)$, are shown in figure 18 for $4 \times 10^{-4} \leqslant k_1\eta \leqslant 1$, which covers the entire inertial and dissipation ranges. It appears that, to within

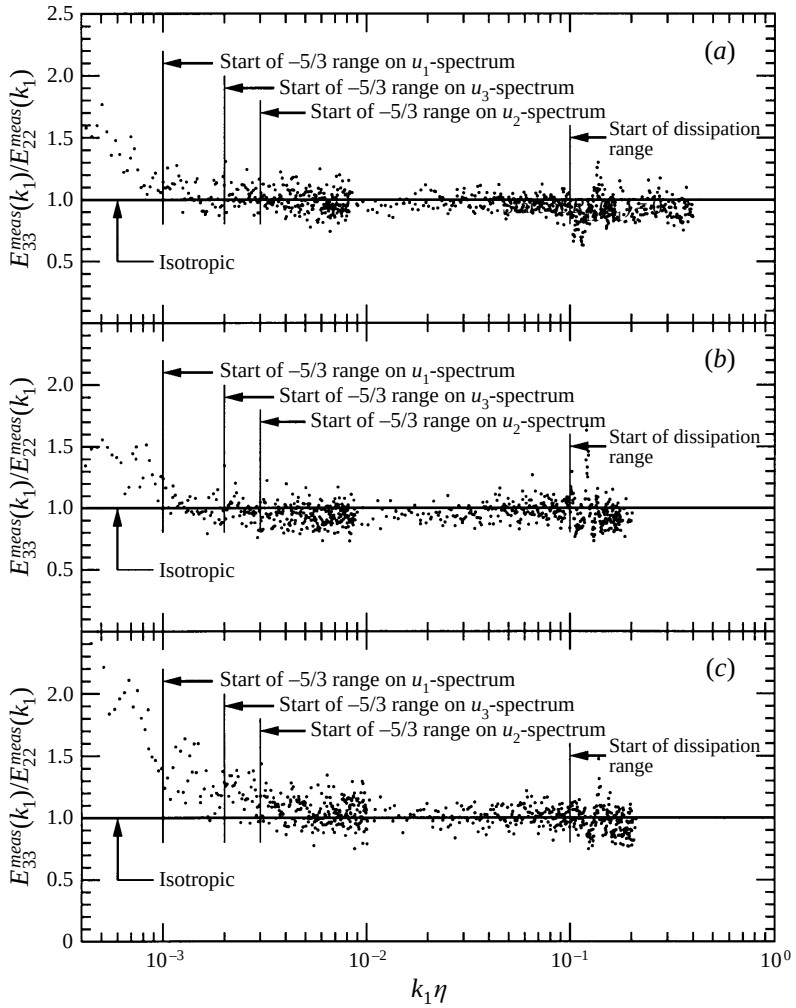

FIGURE 18. Ratios of the measured u_3-spectra to u_2-spectra at different locations in the large-extra-mean-strain rate boundary layer for the high-speed case. For key to captions for (*a–c*) see figure 11.

the accuracy of measurement, at the three locations in the boundary layer the u_3-spectrum becomes equal to the u_2-spectrum (condition *a*) for the wavenumber range of $k_1\eta > 3 \times 10^{-3}$. Similar to I, the transverse spectra, $E_{22}^{calc}(k_1)$ and $E_{33}^{calc}(k_1)$, can be calculated from the measured longitudinal spectrum, $E_{11}^{meas}(k_1)$, using equation (4) of I. An anisotropy measure may be defined as $E_{\alpha\alpha}^{calc}(k_1)/E_{\alpha\alpha}^{meas}(k_1)$, where $\alpha = 2$ or 3 corresponds to u_2 or u_3 respectively. To satisfy condition (*b*), these anisotropy measures should be equal to 1.0 in an isotropic flow. We have used the least-squares-fit data in figures 11, 12 and 13, to calculate these measures, which are shown in figure 19 scaled by the length $(\varepsilon/S^3)^{1/2}$. The data for the plane boundary-layer experiments (I) are also shown in this figure. We again note that the uncertainty in estimating S in the present complex-flow case is larger than the plane-flow experiments. However, it appears that a reasonably good collapse is obtained and local isotropy of energy spectra is achieved ($\pm 10\%$) in the inertial subrange for non-dimensional wavenumbers $k_1(\varepsilon/S^3)^{1/2} > 3$.

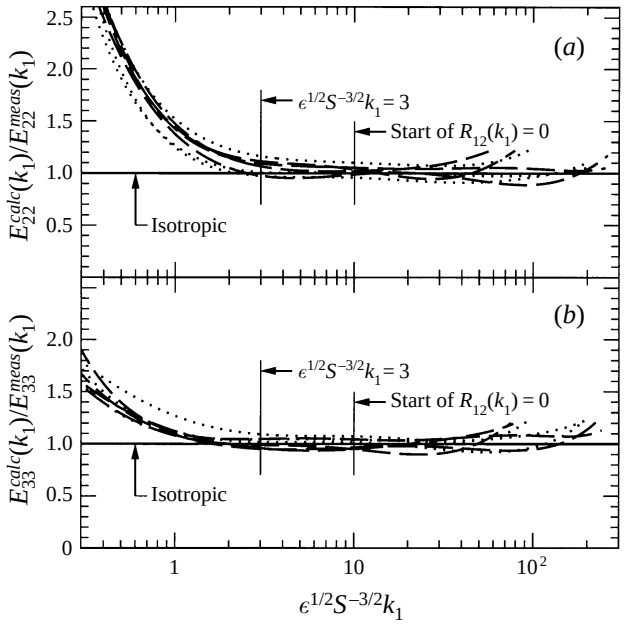

FIGURE 19. Ratios of the calculated to measured transverse spectra. Wavenumber is scaled using the lengthscale $(\varepsilon/S^3)^{1/2}$. (*a*) u_2-ratio; (*b*) u_3-ratio. - - - - -, Plane boundary layer (I) at different locations for high- and low-speed cases; ..... large-extra-mean-strain-rate boundary layer at different locations high-speed case.

Overall, the above spectra and structure functions show that the small-scale behaviour in this high-Reynolds-number ($R_\lambda \approx 2000$) turbulent boundary layer with large extra-mean-strain rate is similar to the zero-pressure-gradient boundary-layer case in I, and that the data are consistent with the local-isotropy predictions.

(ii) *Low-speed experiments*

For the low-speed measurements, we begin our analysis with the dissipation-range spectra because unlike the high-speed case we are able to accurately resolve most of the dissipation ranges. Recall that for this low-speed case we have four measurement stations; $y = 700$, 500, 300 and 100 mm.

The longitudinal dissipation spectra given by the isotropic relation (I, equation (24), Batchelor 1953) are plotted in non-dimensional form in figure 20. These are single-wire data. From the area under each of these curves (before normalization) the dissipation at each position can be calculated. It is clear that for this low-speed case the entire dissipation ranges are obtained. The scatter ($\pm 10\%$) of the data around the peak is the result of superimposing the three measurement segments. Integration over the highest-frequency band (see I for the different frequency bands) for each position, which covered the entire frequency range of interest, gave $\varepsilon \approx 0.19$, 0.53, 0.82 and 2.18 $\mathrm{m^2 s^{-3}}$ for the outer-layer, mid-layer, maximum-stress and inner-layer positions respectively. The microscale Reynolds numbers at these locations are $R_\lambda \approx 670$, 820, 810 and 830 respectively.

To determine the behaviour of the dissipation-range spectra, we show in figure 21 the compensated spectra $\varepsilon^{-2/3}k_1^{5/3}E_{\alpha\alpha}(k_1)$ (where $\alpha = 1$, 2 or 3 and there is no summation over α) at the outer-layer position for $R_\lambda \approx 670$. Recall that at this measurement location we obtained our best spatial resolution of 1.3η. For $k_1\eta > 0.9$

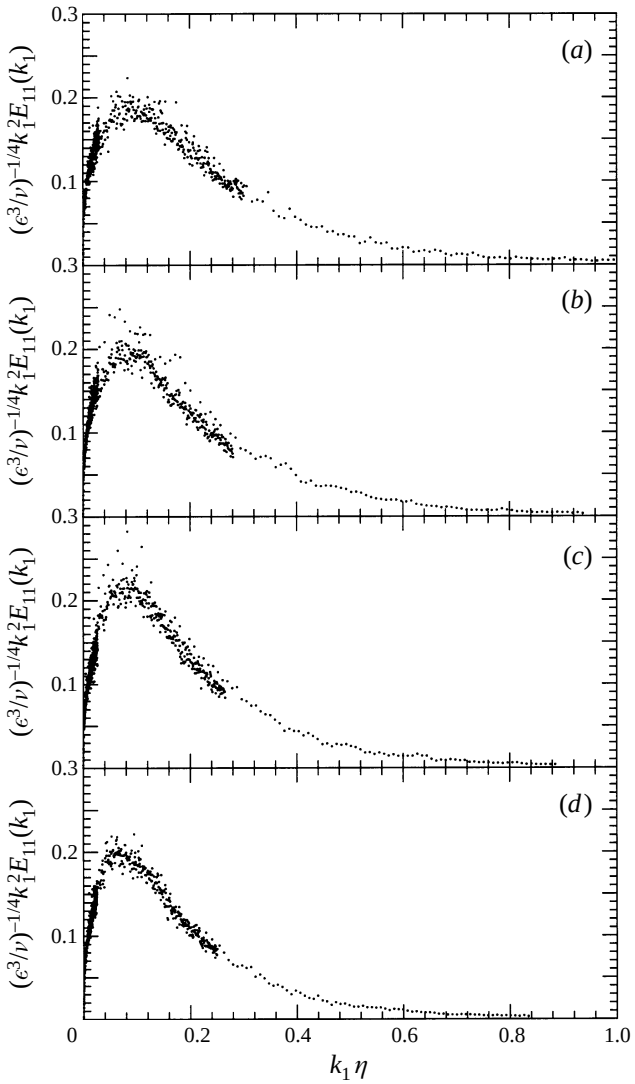

FIGURE 20. Longitudinal dissipation spectra measured at different locations in the large-extra-mean-strain-rate boundary layer for the low-speed case. (*a*) Outer-layer position ($y = 700$ mm, $y^+ \approx 8750$, $R_\lambda \approx 670$). (*b*) Mid-layer position ($y = 500$ mm, $y^+ \approx 6250$, $R_\lambda \approx 820$). (*c*) Maximum-stress position ($y = 300$ mm, $y^+ \approx 3750$, $R_\lambda \approx 810$). (*d*) Inner-layer position ($y = 100$ mm, $y^+ \approx 1250$, $R_\lambda \approx 830$).

the u_1-spectrum (single wire) is affected by noise and/or lack of resolution, but this does not occur in the u_2- and u_3-spectra (crossed-wire). As in I, the data of Comte-Bellot & Corrsin (1971) for isotropic grid turbulence at $R_\lambda = 60.7$ are included in figure 21(*a*) for comparison. The dissipation range of the spectra for the present investigation is very similar to our low-speed plane boundary-layer measurements (see I, figure 11): all spectra of figure 21 have an essentially exponential decay (Kraichnan 1959, see I, equation (25) and the references in I) and follow reasonably well the (DNS) slope $\beta = 5.2$ for $0.5 \leqslant k_1\eta \leqslant 1$. The extent of the agreement between the present u_1-spectrum and Comte-Bellot & Corrsin's data is also similar to I. However,

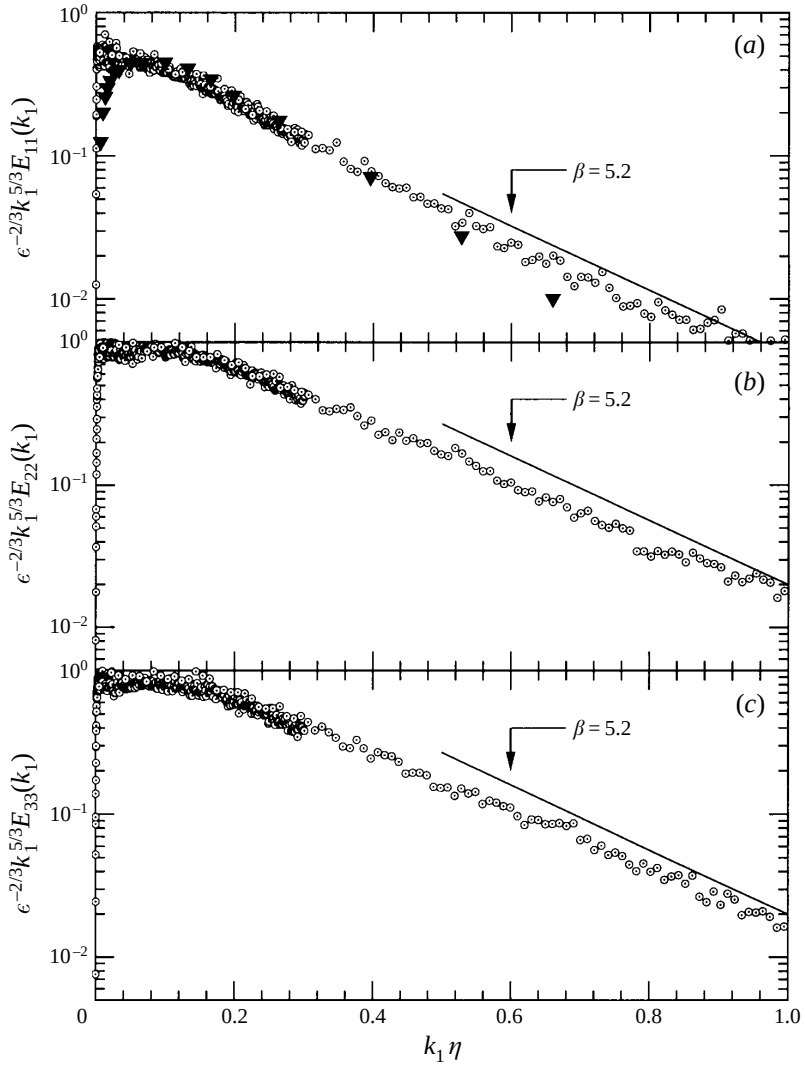

FIGURE 21. Compensated spectra in the dissipation range. (*a*) u_1-spectra; (*b*) u_2-spectrum; (*c*) u_3-spectrum. ⊙, Outer-layer position in the large-extra-mean-strain-rate boundary layer for the low-speed case ($y = 700$ mm, $R_\lambda \approx 670$); ▼, Comte-Bellot & Corrsin (1971) isotropic grid turbulence at $R_\lambda = 60.7$.

in the inertial subrange there are some differences between the transverse spectra of the present low-speed measurements and those of I. These will be addressed below.

In figure 22 the compensated longitudinal spectra at the four positions for the low-speed case are plotted against $k_1\eta$. The compensated ninth-order least-square log-log polynomial fits of $E_{11}(k_1)$ are also included. As described above, the dissipation value used at each measurement location was obtained from the integration of the isotropic dissipation relation (I, equation (24)). The u_1-spectrum (single wire) at each measurement location has approximately one decade of $-\frac{5}{3}$ range and agrees reasonably well with the Kolmogorov constant $C = 1.5$ (i.e. $C_1 = \frac{18}{55}C = 0.491$) (Monin & Yaglom 1975; Saddoughi & Veeravalli 1994; Sreenivasan 1995).

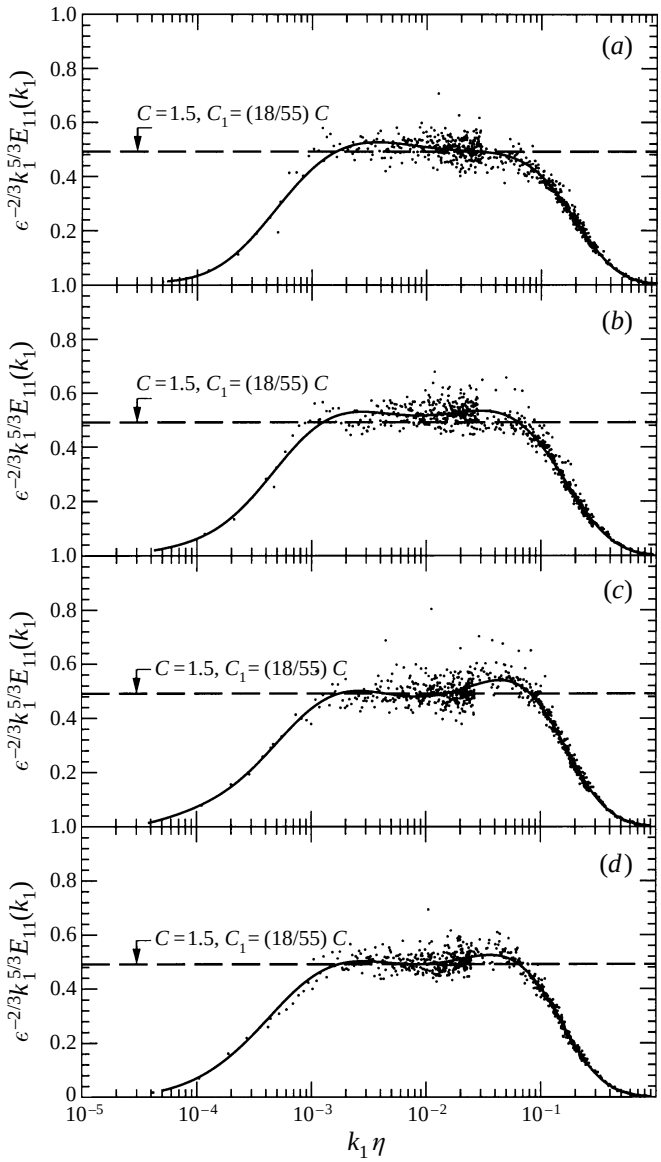

FIGURE 22. Compensated longitudinal (u_1) spectra measured at different locations in the large-extra-mean-strain-rate boundary layer for the low-speed case. Solid lines are the ninth-order, least-square, log-log polynomial fits to the spectral data. For key to captions for (*a–d*) see figure 20.

The compensated u_2- and u_3-spectra for this case are presented in figures 23 and 24 respectively. Recall that the microscale Reynolds numbers at these four measurement locations are reasonably close to each other. Therefore, the differences in the behaviours of spectra at the different locations in the boundary layer may not be attributed to Reynolds-number effects. These two figures illustrate several very important points. (i) They show that the extent of $-\frac{5}{3}$ range of the transverse spectra decreases as the wall is approached. This is similar to the behaviour in the zero-pressure-gradient boundary layer in I. (ii) At the inner-layer position, isotropy is satisfied and the transverse spectra in the inertial subrange are equal to $\frac{4}{3}$ times that

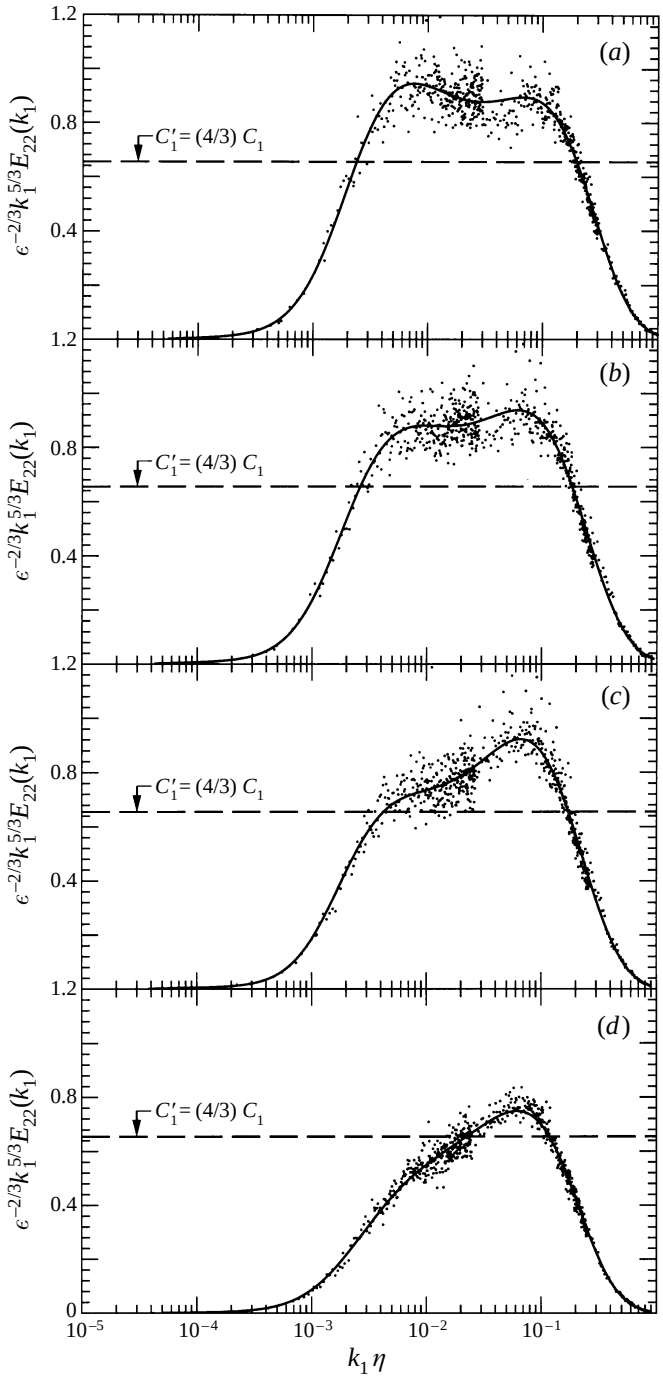

FIGURE 23. As figure 22, but compensated transverse (u_2) spectra.

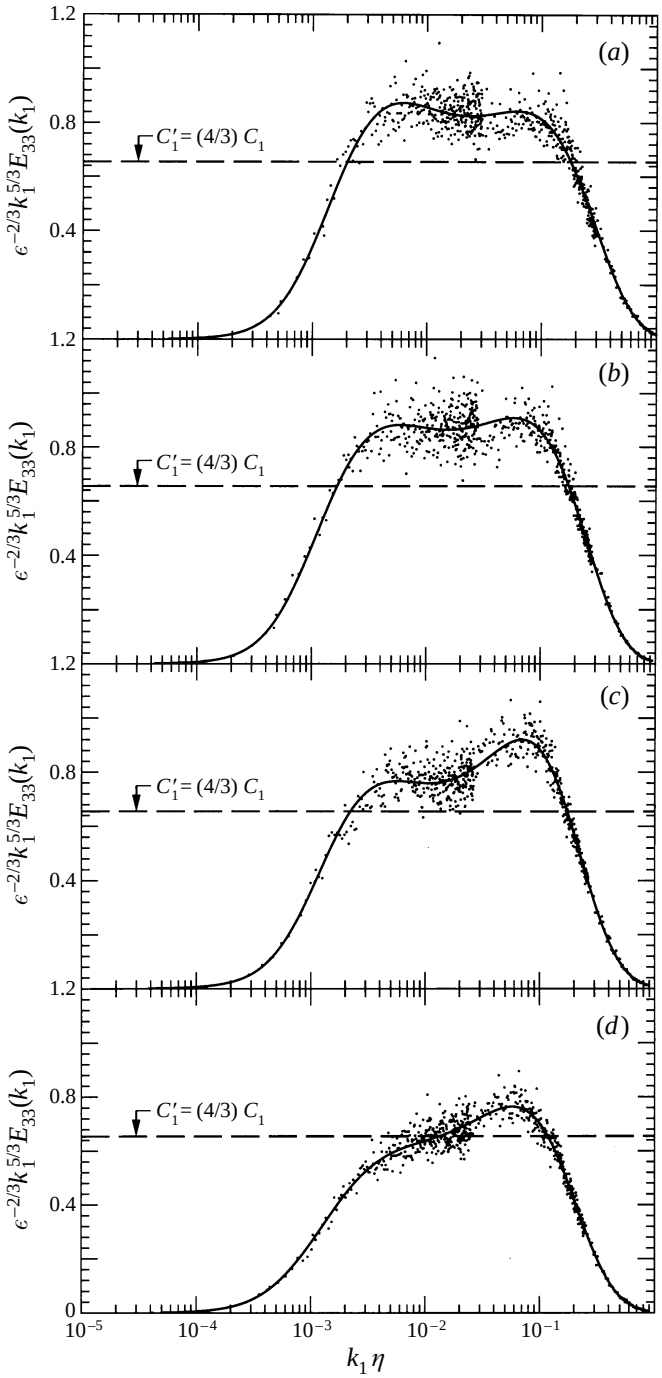

FIGURE 24. As figure 22, but compensated transverse (u_3) spectra.

of the u_1-spectrum. However, as the outer part of the boundary layer is approached, there is an increased deviation from isotropic behaviour. Recall from §3.1.1 and figure 5 that in general the extra mean-strain rates mostly affect the outer part (here 300 mm $\leqslant y \leqslant$ 800 mm or $0.2 \leqslant y/\delta \leqslant 0.6$) of the boundary layer. In this low-speed case we obtain very large values for the shear parameters (see table 1); for example, at $y = 700$ mm, $S_c^* \approx 0.05$ and $S^* \approx 22$, while in our zero-pressure-gradient boundary layer the maximum value for S^* was of the order of 10. In the numerical simulations of shear flows values close to 6 are obtained away from the wall (Lee, Kim & Moin 1990; Borue & Orszag 1996). (iii) All the compensated spectra (see also figure 22) at the outer-layer position ($y = 700$ mm) have a new 'bump' between the large-scale range and the inertial subrange. (iv) At all the measurement positions, to within the accuracy of measurement, the u_3- and u_2-spectra are equal to each other in the inertial subrange and dissipation range, as verified in figure 25, where the ratio of the measured u_3-spectrum to u_2-spectrum, $E_{33}^{meas}(k_1)/E_{22}^{meas}(k_1)$, at each position is plotted against $k_1\eta$.

In figure 26 we present the compensated third-order structure functions for the low-speed case. This figure corresponds to figure 14 for the high-speed case, but here the dissipation values used are those obtained from the spectral measurements. For the high-speed measurements dissipation values were estimated from the third-order structure functions. For the low-speed case this is not done because (i) we could accurately find the dissipation by integrating the dissipation spectrum at each y-location and (ii) no flat regions could be found in the third-order structure functions (figure 26) at low speed, which corresponded to fairly low Taylor microscale Reynolds numbers. However, the overall behaviour of the third-order structure functions in figure 26 is, as expected, similar to those in the zero-pressure-gradient boundary layer: the extent of the inertial range reduces as the wall is approached.

The longitudinal second-order structure functions measured in the low-speed case are shown in figure 27, using the dissipation values obtained from the spectral measurements. They agree very well in the inertial subrange with the Kolmogorov constant $C_2 = 2.0$, which indicates that the dissipation values obtained from the spectral measurements are fairly accurate. Figures 28 and 29 show second-order u_2- and u_3-structure functions respectively. The behaviour of these structure functions in the inertial subrange is similar to the transverse spectra for the low-speed case: at the inner-layer position, isotropy is obtained and the transverse second-order structure functions in the inertial subrange are equal to $\frac{4}{3}$ times the longitudinal structure function. However, as the outer part of the boundary layer is approached, there is an increased deviation from isotropic behaviour. To check the repeatability of the data, all of the low-speed measurements were taken several times on different days with different hot-wire elements having different calibrations and using different anemometers. The run-to-run variations among the data were very small. Also, the u_1-measurements obtained by X-wires in UV- and UW-modes compared well with the data measured by single wires.

Therefore, it appears that our small-scale measurements in a highly distorted turbulent boundary layer with higher-than-normal large-scale intermittency near the edge of the layer at high Reynolds number follow the local-isotropy predictions. For the same flow at low Reynolds number, isotropy is satisfied in the inner-layer position, but in the outer parts of the boundary layer, the small-scale behaviour is perhaps better described as having local axisymmetry about the streamwise direction. There the measured transverse components are equal to each other but they are higher than those the isotropy relations predict. The theory of local

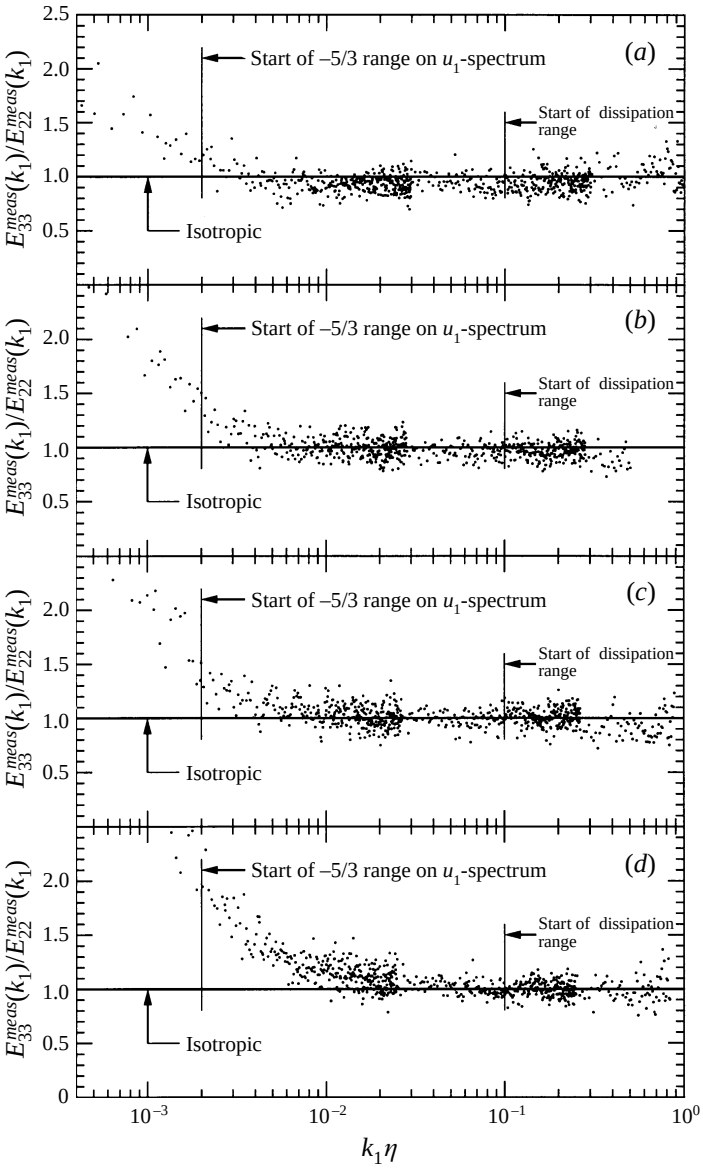

FIGURE 25. Ratios of the measured u_3-spectra to u_2-spectra at different locations in the large-extra-mean-strain-rate boundary layer for the low-speed case. For key to captions for (*a–d*) see figure 20.

axisymmetry – invariance with respect to rotation about a preferred direction – was first introduced by Batchelor (1946) and was later extended by Chandrasekhar (1950).

Hill (1980) discusses the enhancement of the Kolmogorov constant and the inertial-subrange level due to the effects of large-scale intermittency on scalar spectra at high wavenumbers (see also Kuznetsov, Praskovsky & Sabelnikov 1992). Borue & Orszag (1996) found that in their Kolmogorov flow, which is highly intermittent at large scales, the local-isotropy predictions were not satisfied at low Reynolds

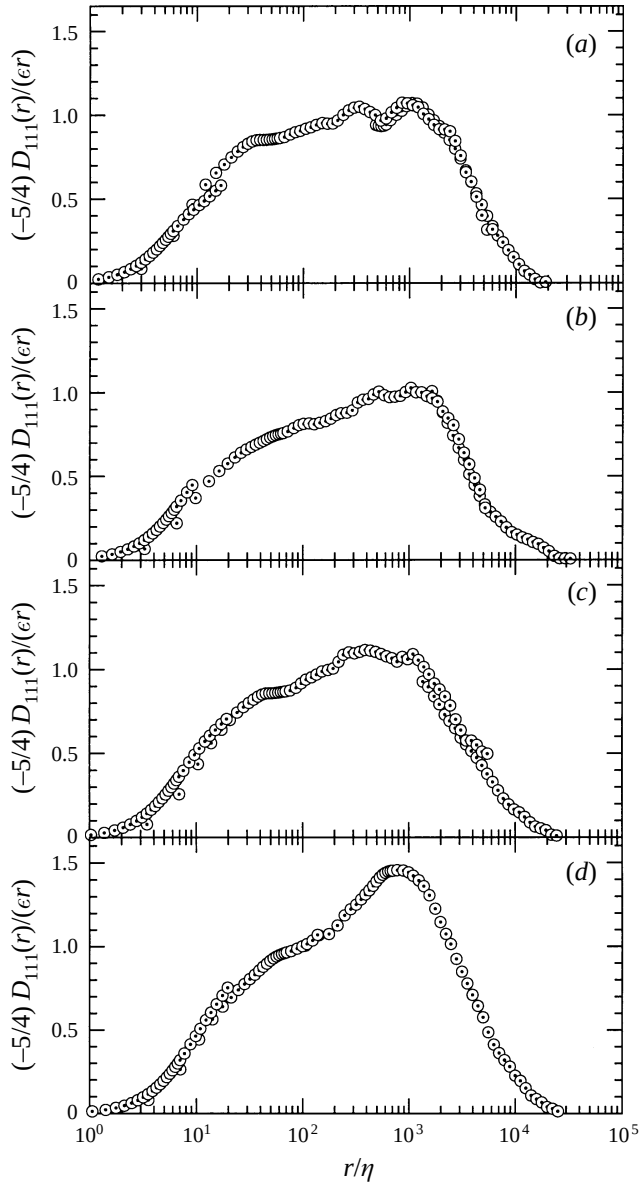

FIGURE 26. Compensated third-order structure functions for longitudinal velocity fluctuations measured at different locations in the large-extra-mean-strain-rate boundary layer for the low-speed case. Dissipation is from the spectral measurements. For key to captions for (*a–d*) see figure 20.

numbers corresponding to numerical resolutions 64^3 and 128^3, but agreement with the predictions was obtained at the numerical resolution 256^3 ($R_\lambda \approx 1000$). Our present results are consistent with our observation in I that as the Reynolds number is decreased, first the transverse and then the longitudinal velocity component variances deviate from Kolmogorov's inertial-range laws at low wavenumbers.

In I, we discussed the importance of analysing linear-log plots of the compensated spectra and structure functions in the inertial subrange. We found that this approach was also required here since the present data again show clearly that without the use

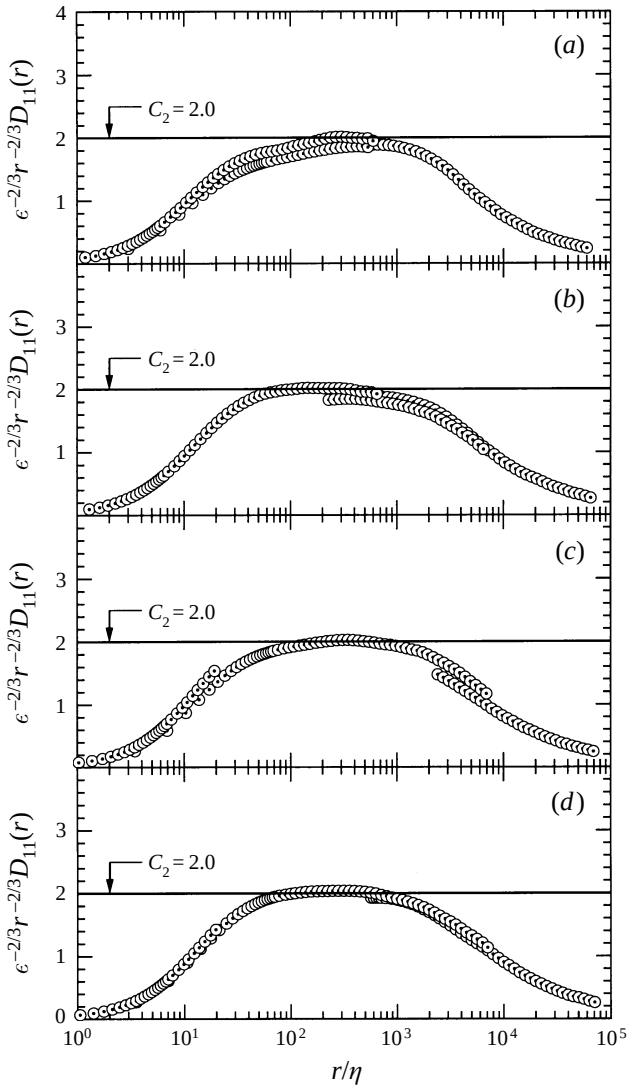

FIGURE 27. Compensated second-order structure functions for longitudinal velocity fluctuations measured at different locations in the large-extra-mean-strain-rate boundary layer for the low-speed case. Dissipation is from the spectral measurements. For key to captions for (*a–d*) see figure 20.

of such plots we would have not been able to see the small deviations from isotropy at low Reynolds numbers.

The correlation-coefficient spectra, $R_{12}(k_1)$ (I, equation (10)), for the low-speed case are plotted in figure 30. The correlation coefficients start their roll-off before the beginning of the $-\frac{5}{3}$ ranges of longitudinal spectra and fall to zero at high wavenumbers at all the measurement locations. However, the isotropic value of zero is obtained only at wavenumbers greater than $k_1\eta \approx 2 \times 10^{-2}$. This is the non-dimensional wavenumber that corresponds to the end of the $-\frac{5}{3}$ range, and the start of the spectral 'bump' on the u_1-spectra (see figure 22). We observed a similar behaviour for the low-Reynolds-number cases in our plane boundary-layer investigations in I. Both positive and negative values are found from the measurements in the high-

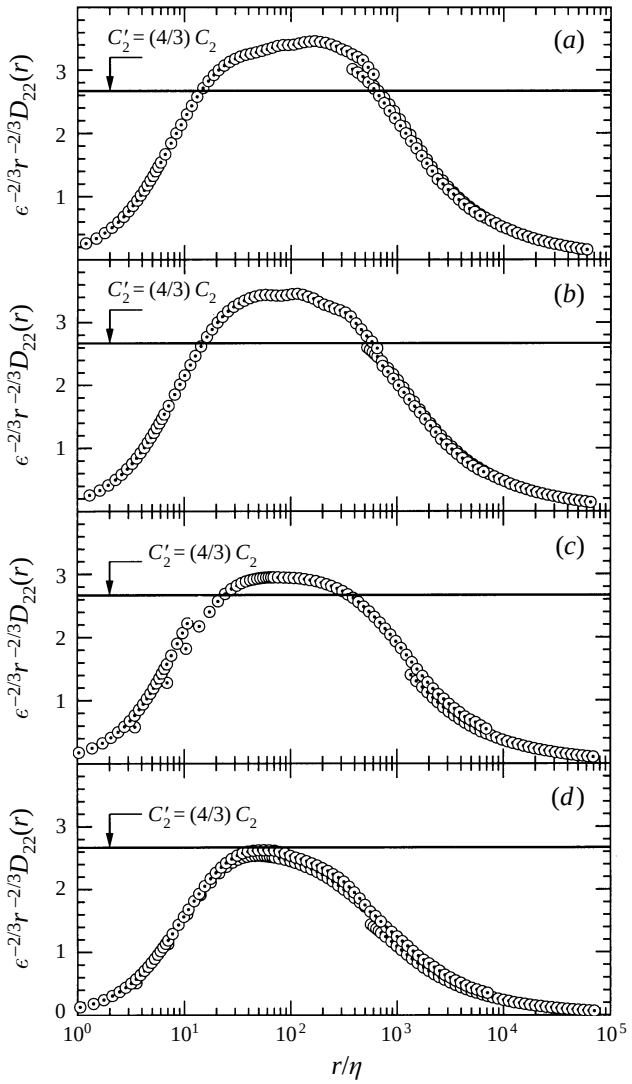

FIGURE 28. As figure 27, but compensated second-order structure functions for transverse (u_2) velocity fluctuations.

wavenumber ranges for all the measurement stations. However, in the dissipation range for the present case, at the measurement locations close to the wall, average values of $R_{12}(k_1)$ appear to be slightly negative. The reasons for this behaviour were discussed earlier and also in I: at the inner-layer station, where the local turbulence intensity is approximately 25%, the errors arising from Taylor's hypothesis can be large in the dissipation range (particularly at low Reynolds numbers, see Heskestad 1965), and the present data appear to follow the trend suggested by Wyngaard & Clifford (1977). However, recently Hill (1996) has shown that Wyngaard & Clifford's formulation greatly overestimates the correction for cospectrum in the dissipation range, but has the correct sign. Recall from table 1 that as the outer-layer stations are approached, the local turbulence intensity decreases and the hot-wire spatial resolution improves. Hence, as seen in figure 30, in the dissipation range of the outer-

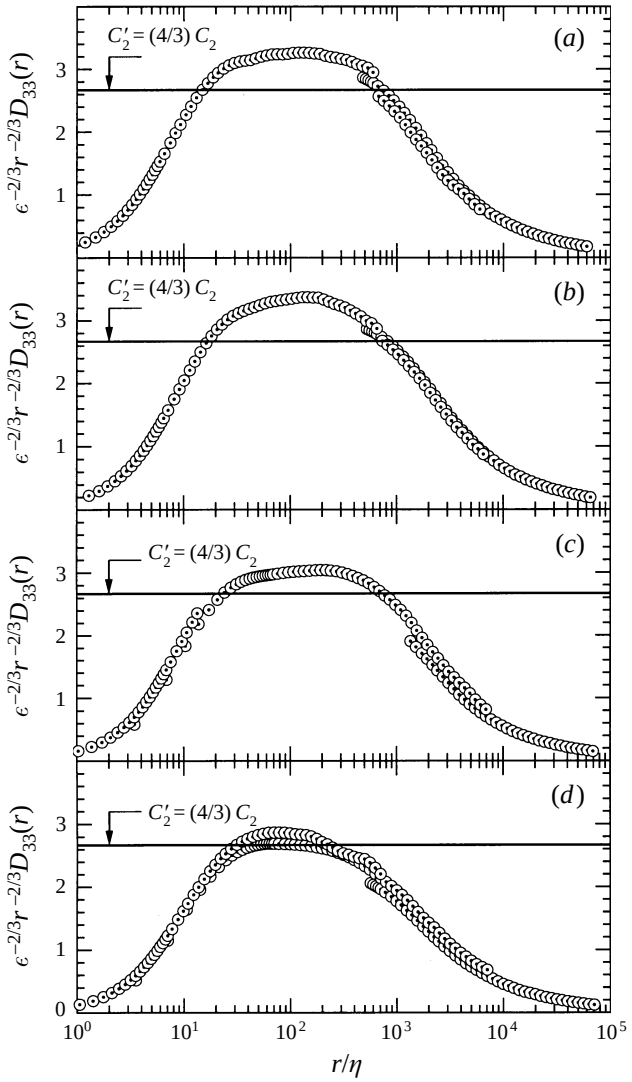

FIGURE 29. As figure 27, but compensated second-order structure functions for transverse (u_3) velocity fluctuations.

layer station ($y = 700$ mm), which had the best spatial resolution (1.3η), the average $R_{12} \approx 0$.

The spectral coherencies defined by equation (11) in I (figure 31), as in I, reach the isotropic value, $H_{12}(k_1) \approx 0$, sooner than the correlation-coefficient spectra.

3.2. *Distorted boundary layers: Small-extra-mean-strain-rate experiments*

In order to isolate the reasons for the slight deviations of the transverse spectra from the local-isotropy predictions in the outer parts of the distorted boundary layer at low Reynolds number, we repeated our measurements at low speed upstream of the cylinder, after the F-18 aircraft was removed from the wind tunnel. In this section only selected data from these measurements will be presented.

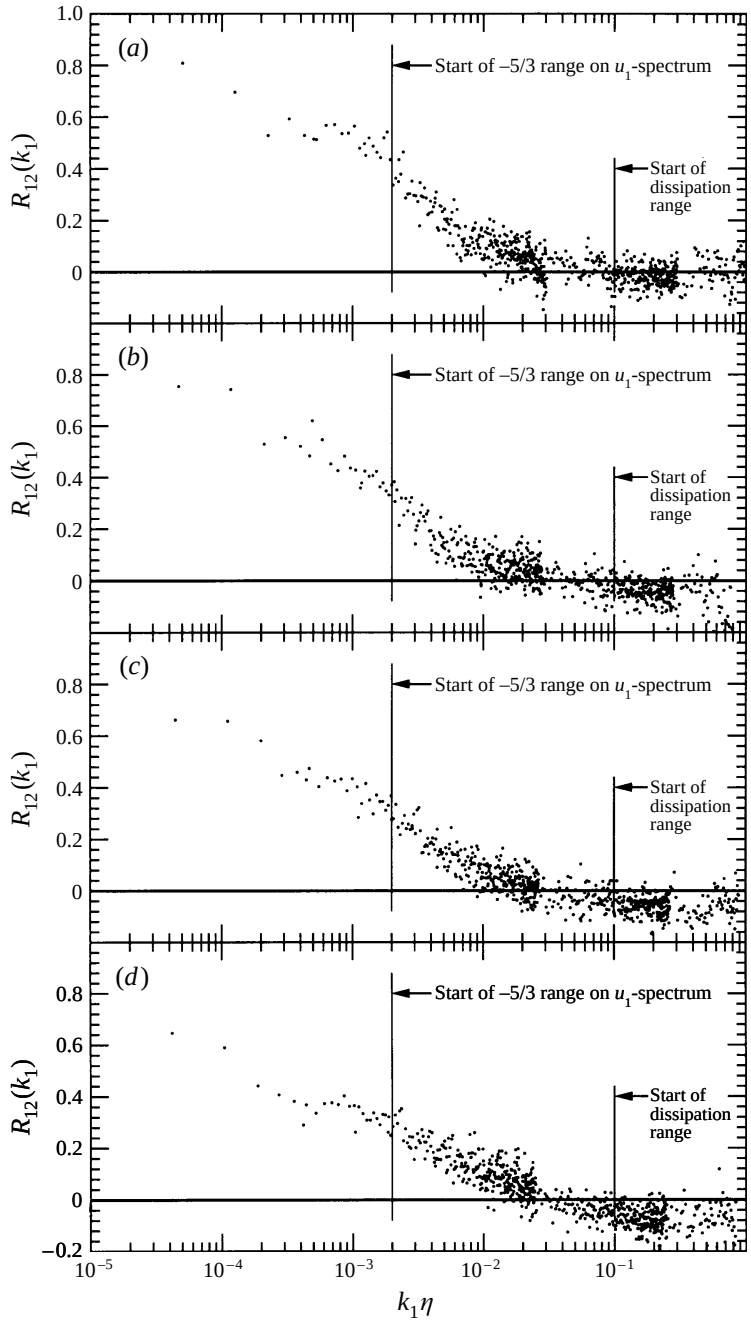

FIGURE 30. Correlation-coefficient spectra measured at different locations in the large-extra-mean-strain-rate boundary layer for the low-speed case. For key to caption for (*a–d*) see figure 20.

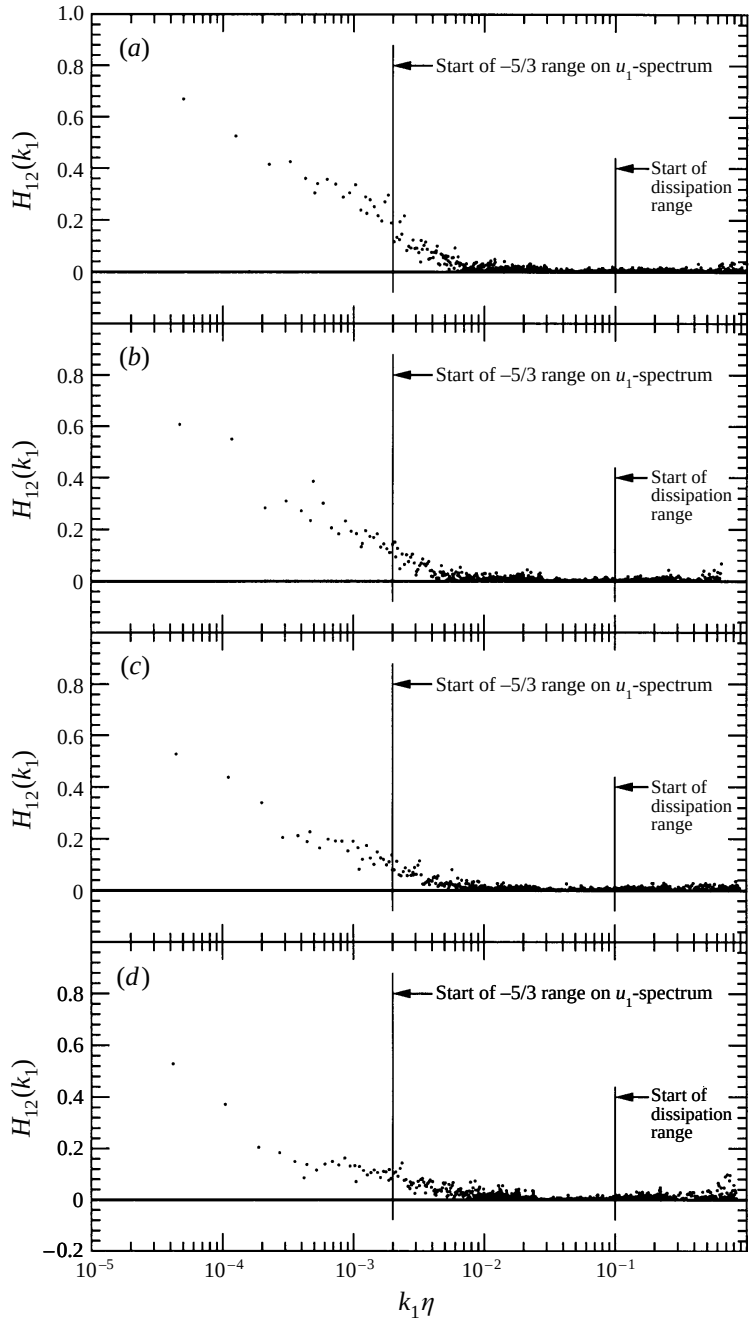

FIGURE 31. Spectral coherency measured at different locations in the large-extra-mean-strain-rate boundary layer for the low-speed case. For key to captions for (*a–d*) see figure 20.

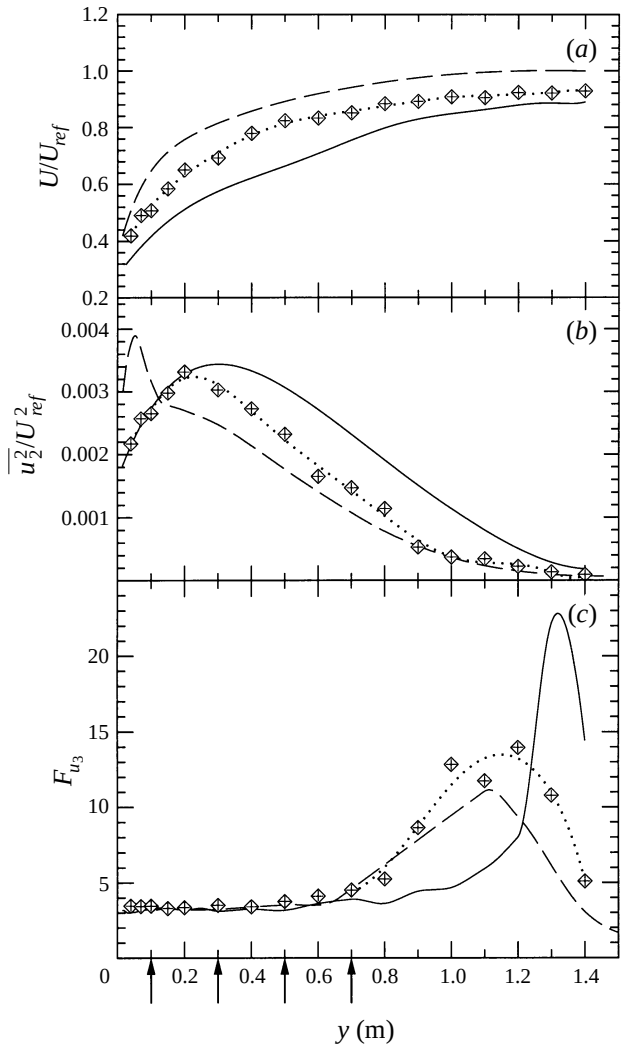

FIGURE 32. Profiles of large-scale data in the small-extra-mean-strain-rate boundary layer at low speed (..... ⊕) compared with plane boundary layer in I (- - - - -) and large-extra-mean-strain-rate boundary layer (———). (*a*) Longitudinal component of mean velocity; (*b*) vertical component of the Reynolds stress; (*c*) spanwise component of the flatness factor.

3.2.1. *Analysis of large-scale data*

The profiles of the longitudinal component of the mean velocity U/U_{ref}, the vertical component of the Reynolds stress $\overline{u_2^2}/U_{ref}^2$, and the spanwise-component flatness factor, $\overline{u_3^4}/(\overline{u_3^2})^2$, are compared in figure 32 with those obtained for the plane boundary layer in I and in the large-extra-mean-strain-rate case (with F-18). It is clear that the removal of the F-18 from the wind tunnel reduces the magnitudes of the extra mean-strain rates. This reduction can be seen in figure 32(*b*), where the vertical component of the Reynolds stress is substantially reduced in the outer parts of the boundary layer. However, the most significant reduction is observed in the large-scale tansverse-velocity flatness factors (e.g. figure 32*c*). This indicates that the

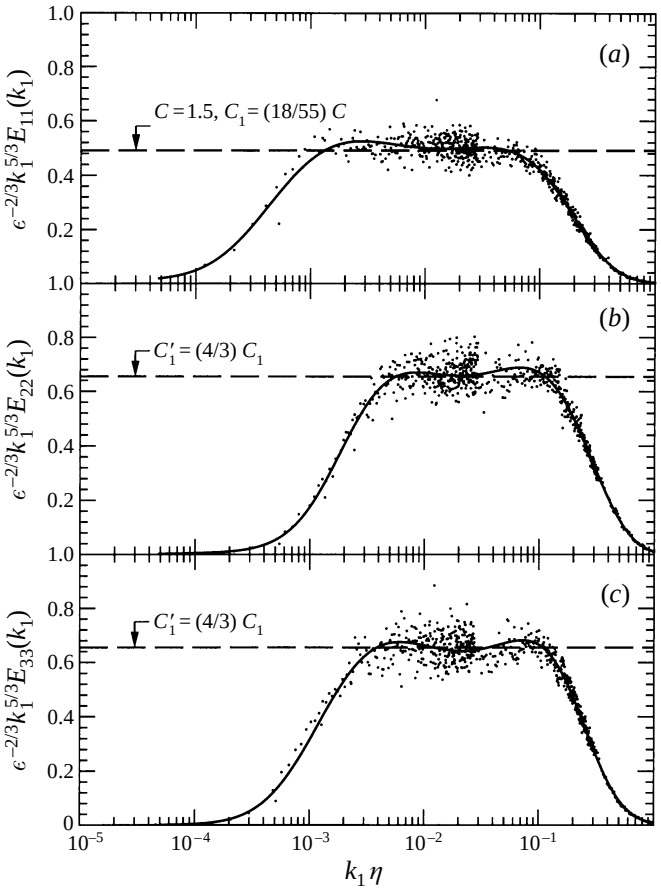

FIGURE 33. Compensated longitudinal and transverse spectra measured at the mid-layer position ($y = 500$ mm) in the small-extra-mean-strain-rate boundary layer at low speed. Solid lines are the ninth-order, least-square, log-log polynomial fits to the spectral data. (*a*) u_1-spectrum; (*b*) u_2-spectrum; (*c*) u_3-spectrum.

highly intermittent signals with sharp spikes near the edge of the distorted boundary layers observed earlier were due to the presence of the F-18 in the wind tunnel.

3.2.2. *Analysis of small-scale data*

Small-scale measurements of the three components of velocity were made at low speed for the three locations in the boundary layer ($y = 300$, 500 and 700 mm) where slight deviations from local-isotropy predictions were observed in transverse spectra at low Reynolds numbers. All these data were completely analysed, but we present here only a small sample of these results. Recall that linear-log plots of the compensated spectra and structure functions proved to be very sensitive tests of local-isotropy predictions in the inertial subrange. Therefore, for the present case we shall only use this type of plot to investigate the isotropy of the small scales.

The compensated longitudinal and transverse spectra taken at the mid-layer location ($y = 500$ mm) and the three components of the compensated second-order structure functions for the outer-layer station ($y = 700$ mm) are shown in figures 33 and 34 respectively. These figures (as well as those not shown here) clearly indicate that, without the F-18 aircraft in the wind tunnel, the transverse spectra and structure

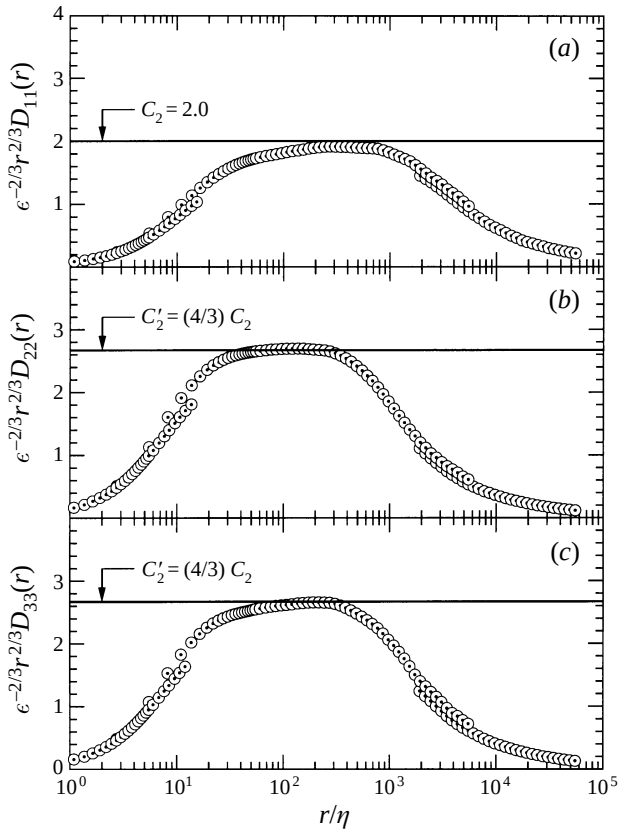

FIGURE 34. Compensated second-order structure functions for longitudinal and transverse velocity fluctuations measured at the outer-layer position ($y = 700$ mm) in the small-extra-mean-strain-rate boundary layer at low speed. (*a*) u_1-structure function; (*b*) u_2-structure function; (*c*) u_3-structure function.

functions in the inertial subrange at all the measurement stations follow the local-isotropy predictions: at each station the transverse components are equal to each other and are larger than the longitudinal component by the $\frac{4}{3}$ factor.

4. General discussion and concluding remarks

At several Reynolds numbers, we have taken hot-wire measurements of the velocity fluctuations in the 1 m thick test-section-ceiling rough-wall boundary layer of the 80 ft $\times$ 120 ft Full-Scale Aerodynamics Facility at NASA Ames Research Center, to test the local-isotropy predictions of Kolmogorov (1941). Our goal has been to obtain accurate small-scale data in a variety of shear flows. To achieve this goal, our experiments were divided into two sets. Our first set of measurements (Saddoughi & Veeravalli 1994, referred to as I) were taken in a 'simple' turbulent boundary layer, with the basic mean strain rate $S(\equiv \partial U/\partial y)$. Our results established the conditions under which local isotropy could be expected in simple shear flows. Among other results, we found that one decade of isotropic inertial subrange requires the ratio of the Kolmogorov to mean-shear timescales, $S_c^*(\equiv S(\nu/\varepsilon)^{1/2})$ (Corrsin 1958; Uberoi 1957) to be not more than about 0.01: for a simple shear layer with turbulent energy production $\approx$ dissipa-

tion, $R_\lambda \approx 1500$. Since then, most of the experimental and computational investigations of the local-isotropy hypothesis have agreed with the results of our study in I.

However, the unanswered question was: would our criteria for the existence of local isotropy in simple shear flows, also hold for 'complex' non-equilibrium flows at high Reynolds numbers? Due to the significant practical importance of complex flows, it was imperative that an answer to the above question be found. The results of these investigations are reported here. We studied the plane-of-symmetry flow upstream of a cylinder placed with its axis perpendicular to the wall (for example, representing the flow in the vicinity of a wing–body junction). In this flow configuration the pressure rises strongly as the obstacle is approached and in the plane of symmetry the boundary layer is influenced by the effects of lateral divergence. The extra mean strain rates involved are $\partial U/\partial x$, $\partial V/\partial y$ and $\partial W/\partial z$ (in the plane of symmetry $\partial V/\partial x$ was assumed to be small).

The desired effects can be obtained only if the size of the cylinder is at least of the order of the approaching boundary-layer thickness. Hence, our cylinder had the following dimensions: $D = 1.22$ m and height $L = 1.83$ m. During all our complex-flow measurements the tunnel runs were dedicated to our experiments. However, a full-scale F-18 fighter aircraft set at an angle of attack of 50° was present in the central region of the working section for both of our high- and low-speed measurements. To identify the effects of the aircraft on the flow characteristics, measurements were repeated with the tunnel empty. The presence of the aircraft in the tunnel usefully increased the magnitude of the mean strain rates upstream of the cylinder. Therefore, our complex-flow experiments were divided into two cases: boundary layers under the influence of (i) large and (ii) small extra mean-strain rates, which corresponded respectively to measurements upstream of the cylinder (i) with and (ii) without the F-18 in the wind tunnel. The results of these experiments were compared with those from our plane boundary-layer study (I).

In the large-extra-mean-strain-rate case, the boundary-layer thickness at the single longitudinal measurement station increased to 1.35 m. The maximum Reynolds numbers based on momentum thickness, R_θ, and on Taylor microscale, R_λ, were approximately 510 000 and 2000 respectively. These are the largest attained in laboratory boundary-layer flows: R_θ is of the same order obtained in flight on a typical commercial aircraft or the space shuttle (Gad-el-Hak & Bandyopadhyay 1994). In the middle of the boundary layer, typical values of the extra-mean-strain-rate parameters were $e/(\partial U/\partial y) \geqslant 0.6$: these are very large values and produce large nonlinear effects on the large-scale structures of the boundary layers (Bradshaw 1973). Compared with the plane turbulent boundary-layer case (I) these effects are: (i) the longitudinal mean-velocity profile becomes flatter in the middle of the layer, (ii) the Reynolds-stress maxima move away from the wall to $y \approx 300$ mm (in the outer part of the boundary layer the values of all these stresses increase), and (iii) Townsend's (1976) structure parameter $a_1(\equiv -\overline{u_1 u_2}/q^2)$ drops to very low values in the inner part of the boundary layer, but recovers its canonical value (≈ 0.13) in the outer part of the layer (see Bradshaw 1967). Furthermore, the large-scale skewness and flatness factors indicated that the fluctuating signals near the edge of the boundary layers were more intermittent and had sharper spikes than in I.

Small-scale measurements were conducted at four locations in the boundary layer, and they are referred to as the inner-layer, maximum-stress, mid-layer and outer-layer positions. The maximum values for the shear-rate parameters, $S^*(\equiv Sq^2/\varepsilon)$, and S_c^* were about 22 and 0.05 respectively, where for the present experiments $S \equiv 2(s_{ij}s_{ij}/2)^{1/2}$. Expressions given by Wyngaard & Clifford (1977), based on the

work of Lumley (1965), were again used to estimate the errors arising from the use of Taylor's hypothesis. For the wavenumbers of interest, except in the dissipation range at the inner-layer position, these errors were small and no correction was applied to any of the present data.

At high Reynolds numbers ($R_\lambda \approx 2000$) spectra and structure functions in the inertial subrange for all the measurement stations behaved similarly to those in the plane boundary-layer experiments (I) and were consistent with the local-isotropy predictions. Also, as in I, the shear-stress cospectral density $E_{12}(k_1)$ rolled-off with a $-\frac{7}{3}$ power law and scaled linearly with S (Lumley 1967). We obtained the same value as I of the constant for cospectra, $C_0 \approx 0.15$ (Wyngaard & Cote 1972), and the correlation-coefficient spectra $R_{12}(k_1)$ decayed algebraically (Nelkin & Nakano 1983; Saddoughi & Veeravalli 1994; Borue & Orszag 1996).

In general, at low Reynolds numbers ($R_\lambda \approx 800$) the data behaved similarly to I: the energy spectra exhibited exponential decay in the dissipation range (Kraichnan 1959), the correlation-coefficient spectra started their roll-off before the beginning of the $-\frac{5}{3}$ ranges in longitudinal spectra and fell to zero at high wavenumbers, and the spectral coherencies reached the isotropic value, $H_{12}(k_1) \approx 0$, sooner than the correlation-coefficient spectra. The isotropic relation was used to obtain the dissipation at each measurement location. In the inertial subrange, the generally accepted Kolmogorov constants for the longitudinal spectrum, $C_1 \approx 0.5$, and the second-order structure function, $C_2 \approx 2$ (Monin & Yaglom 1975; Saddoughi & Veeravalli 1994; Sreenivasan 1995) were obtained.

At each measurement location, the compensated transverse spectra (and second-order structure functions) were equal to each other, implying local axisymmetry about the streamwise direction (Batchelor 1946; Chandrasekhar 1950). At the inner-layer position, isotropy was satisfied and the measured transverse components in the inertial subrange were equal to $\frac{4}{3}$ times that of the measured longitudinal component. However, as the outer part of the boundary layer was approached there was an increased deviation from isotropic behaviour. This was attributed to low-Reynolds-number effects, since our small-scale measurements in the same highly distorted turbulent boundary layer (with higher-than-normal large-scale intermittency near the edge of the layer) at high Reynolds number followed the local-isotropy predictions at all the measurement locations. Hill (1980) discusses the enhancement of the inertial subrange level due to the effects of large-scale intermittency on scalar spectra, and Borue & Orszag (1996) found that in their Kolmogorov flow, which is highly intermittent at large scales, the local-isotropy predictions were not satisfied at low Reynolds numbers, but agreement with the predictions was obtained at high Reynolds number.

The low-speed measurements were repeated, after the F-18 aircraft was removed from the wind tunnel. These data indicated reductions in the magnitudes of the extra mean-strain rates. The Reynolds stresses were reduced in the outer parts of the boundary layer, and significant reductions were observed in the large-scale tansverse flatness factors measured near the edge of the boundary layer. These low-Reynolds-number data showed that the transverse spectra and second-order structure functions at all the measurement locations followed the local-isotropy predictions. In I we discussed the importance of analysing linear-log plots of the compensated spectra and structure functions. We found that it was imperative that this approach be adopted here also, since the present data showed clearly that without the use of such plots, we would have not been able to see the intricate behaviour of the inertial subrange.

In summary, the current investigations confirm the conclusions of our earlier study (I) and show that one decade of locally isotropic inertial subrange requires the ratio of

the Kolmogorov to mean-shear timescales, S_c^*, of not more than approximately 0.01. However, in the present non-equilibrium boundary layer, this condition required a higher Reynolds number ($R_\lambda \approx 2000$) than in I ($R_\lambda \approx 1500$). Overall, our complex-flow experiments have again highlighted an important fact: as long as the high-Reynolds-number requirement – which is an intrinsic part of the local-isotropy hypothesis – is satisfied, the small-scale structures of turbulent motions become independent of large-scale structures and the mean deformation rate (Kolmogorov 1941).

We wish to thank, Drs Fredric Schmitz and James Ross of the Full-Scale Aerodynamics Research Division at NASA Ames for permitting us to use the 80 ft × 120 ft wind tunnel and the other facilities. Our experiments would have not been possible without their help and the efforts of all the staff of the Division.

Professor Bill Reynolds helped me with the design and construction of the test cylinder, and also provided many ideas pertaining to data analysis and the design of new experiments. I discussed many aspects of these experiments, particularly the effects of extra mean strain rates, with Professor Peter Bradshaw. For the last few years, Dr Bob Rogallo has corrected the manuscripts for these experiments and suggested ways to analyse the data. Throughout the course of these experiments I have had many valuable discussions with Professor Parviz Moin; he has been a constant source of inspiration and support. I would like to thank them all for their selfless help and efforts.

I have also dicussed these results with Professors George Batchelor, Peter Joubert, Roger Simpson, Bill George, Javier Jimenez, Sanjiva Lele, Dale Pullin, John Kim, Paul Durbin, and Drs Nagi Mansour, Reginald Hill and Erik Lindborg. I thank them all for their help and advice.

I am also grateful to my wife, Elizabeth, and Eric Buice, who helped me with the measurements during all those 'graveyard' shifts at NASA Ames.

REFERENCES

Antonia, R. A., Zhu, Y., Anselmet, F. & Ould-Rouis, M. 1996 Comparison between the sum of second-order velocity structure functions and the second-order temperature structur function. *Phy. Fluids* **8**, 3105–3111.

Antonia, R. A., Zhu, Y. & Shafi, H. S. 1996 Lateral vorticity measurements in a turbulent wake. *J. Fluid Mech* **323**, 173–200.

Batchelor, G. K. 1946 The theory of axisymmetric turbulence. *Proc R. Soc. Lond* A **186**, 480–502.

Batchelor, G. K. 1953 *The Theory of Homogeneous Turbulence*. Cambridge University Press.

Belik, L. 1973 The secondary flow about circular cylinders mounted normal to a flat plate. *Aero Q*. **24**, 47–54.

Borue, V. & Orszag, S. A. 1996 Numerical study of three-dimensional Kolmogorov flow at high Reynolds numbers. *J. Fluid Mech.* **306**, 293–323.

Bradshaw, P. 1967 The turbulence structure of equilibrium boundary layers. *J. Fluid Mech.* **29**, 625–645.

Bradshaw, P. 1969 Conditions for the existence of an inertial subrange in turbulent flows. *Aero. Res. Council R. & M*. 3603. NPL, London.

Bradshaw, P. 1973 Effects of streamline curvature on turbulent flow. *AGARDograph* **169**.

Bradshaw, P. 1994 Turbulence: the chief outstanding difficulty of our subject. *Exps. Fluids* **16**, 203–216.

Canuto, V. M. & Dubovikov, M. S. 1996*a* A dynamical model for turbulence. I. General formalism. *Phys. Fluids* **8**, 571–586.

Canuto, V. M. & Dubovikov, M. S. 1996*b* A dynamical model for turbulence. II. Shear-driven flows. *Phys. Fluids* **8**, 587–598.

Canuto, V. M., Dubovikov, M. S., Cheng, Y. & Dienstfrey, A. 1996 A dynamical model for turbulence. III. Numerical results. *Phys. Fluids* **8**, 599–613.

Chandrasekhar, S. 1950 The theory of axisymmetric turbulence. *Proc R. Soc. Lond.* A **242**, 557–577.

Chapman, D. 1979 Computational aerodynamics development and outlook. *AIAA J.* **17**, 1293.

Comte-Bellot, G. & Corrsin, S. 1971 Simple Eulerian time correlation of full and narrow-band velocity signals in grid-generated 'isotropic' turbulence. *J. Fluid Mech.* **48**, 273–337.

Corrsin, S. 1958 On local isotropy in turbulent shear flow. *NACA R & M* 58B11.

Devenport, W. J. & Simpson, R. L. 1990 Time-dependent and time-averaged turbulence structure near the nose of a wing-body junction. *J. Fluid Mech.* **210**, 23–55.

Falkovich, G. 1994 Bottleneck phenomenon in developed turbulence. *Phys. Fluids* **6**, 1411.

Fernholz, H. H. & Finley, P. J. 1996 The incompressible zero-pressure-gradient turbulent boundary layer: An assessment of the data. *Prog. Aerospace Sci.* **32**, 245–311.

Fernholz, H. H., Krause, E., Nockemann, M. & Schober, M. 1995 Comparative measurements in the canonical boundary layer at $Re_{\delta 2} \leqslant 6 \times 10^4$ on the wall of the DNW. *Phys. Fluids* A **7**, 1275–1281.

Freymuth, P. 1968 Noise in hot-wire anemometers. *Rev. Sci. Instrum*, **10**, 550–557.

Frisch, U. 1995 *Turbulence*. Cambridge University Press.

Gad-el-Hal, M. & Bandyopadhyay, P. 1994 Reynolds number effects in wall-bounded flows. *Appl. Mech. Rev.* **47**, 307–365.

Grossmann, S., Lohse, D., Lvov, V. & Procaccia, I. 1994 Finite size corrections to scaling in high Renolds number turbulence. *Phys. Rev. Lett.* **73**, 432–435.

Head, M. R. & Patel, V. C. 1968 Improved entrainment method for calculating turbulent boundary layer development. *ARC R & M* 3643.

Heskestad, G. 1965 A generalized Taylor hypothesis with application for high Reynolds number turbulent shear flows. *J. Appl. Mech.* **87**, 735–739.

Hill, R. J. 1980 Effects of large-scale intermittency of turbulence on scalar spectra at high wavenumbers. *NOAA Tech. Rep. ERL* 409-WPL 54.

Hill, R. J. 1996 Corrections to Taylor's frozen turbulence approximation. *Atmos. Res.* **40**, 153–175.

Hill, R. J. & Wilczak, J. M. 1995 Pressure structure functions and spectra for locally isotropic turbulence. *J. Fluid Mech.* **296**, 247–269.

Hornung, H. G. & Joubert, P. N. 1963 The mean velocity profile in three-dimensional turbulent boundary layers. *J. Fluid Mech.* **15**, 368–384.

Hunt, J. C. R., Phillips, O. M. & Williams, D. (eds.) 1991 Turbulence and stochastic processes: Kolmogorov's ideas 50 years on. *Proc. R. Soc. Lond.* A **434**.

Johnston, J. P. 1960 The turbulent boundary layer at a plane of symmetry in a three-dimensional flow. *Trans. ASME* D: **82,** 622–628.

Klebanoff, P. S. 1954 Characteristics of turbulence in a boundary layer with zero pressure gradient. *NACA Tech. Note* 3178.

Kolmogorov, A. N. 1941 The local structure of turbulence in incompressible viscous fluid for very large Reynolds numbers. *C. R. Acad. Sci. URSS* **30**, 301.

Kraichnan, R. H. 1959 The structure of isotropic turbulence at very high Reynolds numbers. *J. Fluid Mech.* **5**, 497.

Kuznetsov, V. R., Praskovsky, A. A. & Sabelnikov, V. A. 1992 Fine-scale turbulence structure of intermittent shear flows. *J. Fluid Mech.* **243**, 595–622.

Lee, M. J., Kim, J. & Moin, P. 1990 Structure of turbulence at high shear rate. *J. Fluid Mech.* **216**, 561–583.

Lee, M. J. & Reynolds, W. C. 1985 Numerical experiments on the structure of homogeneous turbulence. *Tech. Rep.* TF-24. Department of Mechanical Engineering, Stanford University.

Lindborg, E. 1995 Kinematics of homogeneous axisymmetric turbulence. *J. Fluid Mech.* **302**, 179–201.

Lindborg, E. 1996 A note on Kolmogorov's third-order structure function law, local-isotropy hypothesis and the pressure-velocity correlation. *J. Fluid Mech.* **326**, 343–356.

Lohse, D. & Muller-Groeling, A. 1995 Bottleneck effects: scaling phenomena in r- versus p-space. *Phys. Rev. Lett.* **74**, 1747–1750.

Lumley, J. L. 1965 Interpretation of time spectra measured in high-intensity shear flows. *Phys. Fluids* **8**, 1056.

Lumley, J. L. 1967 Similarity and the turbulent energy spectrum. *Phys. Fluids* **10**, 855–858.

MEHTA, R. D. 1984 Effect of wing nose shape on the flow in a wing/body junction. *Aeronaut. J.* **88**, 456–460.

MILLER, P. L. & DIMOTAKIS, P. E. 1996 Measurements of scalar power spectra in high Schmidt number turbulent jets. *J. Fluid Mech* **308**, 129–146.

MOIN, P. 1990 Similarity of organized structures in turbulent shear flows. In *Near-Wall Turbulence* (ed. S. J. Kline & N. H. Afgan), p. 2. Hemisphere.

MONIN, A. S. & YAGLOM, A. M. 1975 *Statistical Fluid Mechanics*, vol. 2. MIT Press.

MYDLARSKI, L. & WARHAFT, Z. 1996 On the onset of high-Reynolds-number grid-generated wind-tunnel turbulence. *J. Fluid Mech.* **320**, 331–368.

NELKIN, M. 1994 Universality and scaling in fully developed turbulence. *Adv. Phys.* **43**, 143–181.

NELKIN, M. & NAKANO, T. 1983 How do the small scales become isotropic in Navier-Stokes turbulence. In *Turbulence and Chaotic Phenomena in Fluids* (ed. T. Tatsumi), p. 319. Elsevier.

PUMIR, A. 1996 Turbulence in homogeneous shear flows. *Phys. Fluids* **8**, 3112–3127.

PUMIR, A. & SHRAIMAN, B. I. 1995 Persistent small-scale anisotropy in homogeneous shear flows. *Phys. Rev. Lett.* **75**, 3114–3116.

PURTELL, P. 1992 Turbulence in complex flows: a selected review. *AIAA Paper* 92-0435.

SADDOUGHI, S. G. 1989 Some selected contributions from Peter N. Joubert and his students to the study of perturbed turbulent boundary layers. *10th Australasian Fluid Mech. Conf., University of Melbourne.*

SADDOUGHI, S. G. 1993 Local isotropy in distorted turbulent boundary layers at high Reynolds number. *Annual Research Briefs of the Center for Turbulence Research*, pp. 347–363. Stanford University/NASA Ames.

SADDOUGHI, S. G. 1994 Small-scale behaviour in distorted turbulent boundary layers at low Reynolds number. *Annual Research Briefs of the Center for Turbulence Research.* pp. 243–261. Stanford University/NASA Ames.

SADDOUGHI, S. G. 1995 Small-scale behaviour in distorted turbulent boundary layers at high Reynolds number. Lecture Notes in Physics, vol. 462 (ed. M. Meneguzzi, A. Pouquet & P. L. Sulem), pp. 3–9. Springer.

SADDOUGHI, S. G. & JOUBERT, P. N. 1991 Lateral straining of turbulent boundary layers. Part 1. Streamline divergence. *J. Fluid Mech.* **229**, 173–204.

SADDOUGHI, S. G. & VEERAVALLI, S. V. 1994 Local isotropy in turbulent boundary layers at high Reynolds number. *J. Fluid Mech.* **268**, 333–372 (referred to herein as I).

SADDOUGHI, S. G. & VEERAVALLI, S. V. 1996 Hot-wire anemometry behaviour at very high frequencies. *Meas. Sci. Technol.* **7**, 1297–1300.

SHILOH, K., SHIVAPRASAD, B. G. & SIMPSON, R. L. 1981 The structrue of a separating turbulent boundary layer. Part 3. Transverse velocity measurements. *J. Fluid Mech.* **113**, 75–90.

SIMPSON, R. L., CHEW, Y. T. & SHIVAPRASAD, B. G. 1981 The structure of a separating turbulent boundary layer. Part 2. Higher-order turbulence results. *J. Fluid Mech.* **113**, 53–73.

SMITH, C. R., WALKER, J. D. A., HAIDARI, A. H. & SOBRUN, U. 1991 On the dynamics of near-wall turbulence. *Phil. Trans. R. Soc. Lond.* A **336**, 131–175.

SMITS, A. J. & WOOD, D. H. 1985 The response of turbulent boundary layers to sudden perturbations. *Ann. Rev. Fluid Mech.* **17**, 321–358.

SREENIVASAN, K. R. 1995 On the universality of the Kolmogorov constant. *Phys. Fluids* **7**, 2778–2784.

TAYLOR, G. I. 1935 Statistical theory of turbulence. *Proc. R. Soc. Lond.* A **151**, 421.

TOWNSEND, A. A. 1976 *The Structure of Turbulent Shear Flow*, 2nd edn. Cambridge University Press.

UBEROI, M. S. 1957 Equipartition of energy and local isotropy in turbulent flows. *J. Appl. Phys.* **28**, 1165–1170.

WYNGAARD, J. C. & CLIFFORD, S. F. 1977 Taylor's hypothesis and high-frequency turbulence spectra. *J. Atmos. Sci.* **34**, 922–929.

WYNGAARD, J. C. & COTE, O. R. 1972 Co-spectral similarity in the atmospheric surface layer. *Q. J. R. Met. Soc.* **98**, 590–603.

YAGLOM, A. M. 1994 A. N. Kolmogorov as a fluid mechanician and founder of a school in turbulence research. *Ann. Rev. Fluid Mech.* **26**, 1–22.

YAKHOT, V. 1994 Large-scale coherence and 'anomalous scaling' of higher-order moments of velocity differences in strong turbulence. *Phys. Rev.* E **49**, 2887.

ZAGAROLA, M. V., SMITS, A. J., ORSZAG, S. A. & YAKHOT, V. 1996 Experiments in high Reynolds number turbulent pipe flow. *AIAA Paper* 96–0654.